Part II

Tropical Cyclones

8. Overview of Tropical Cyclones

8.1. Definition

What, exactly, is a tropical cyclone? According to the American Meteorological Society Glossary, *tropical cyclone* is “the general term for a cyclone that originates over the tropical oceans”. But for our purposes, this definition is at once too broad and too restrictive. Not all cyclones that form over tropical oceans operate by the same physical mechanism. For example, in winter, some baroclinic cyclones form in the tropics. On the other hand, certain types of polar low and medicanes (nearly circular cyclones that occasionally develop over the Mediterranean Sea) operate on essentially the same mechanism as conventional tropical cyclones yet they develop outside the tropics. And “agukabams” whose appearance in satellite imagery is nearly identical to classical tropical cyclones, develop over land. In models, tropical cyclone-like vortices develop in dry adiabatic atmospheres free of any water vapor; thus moist convection plays no role in these cyclones.

What unites these various phenomena is that they are all powered by surface enthalpy fluxes. This book is about the physics of such storms, and thus for our purposes, the term *tropical cyclone* will be taken to apply to *any cyclonic vortex powered primarily by enthalpy fluxes from the surface*. As with any formal definition, there are drawbacks. As mentioned above, the modifier “tropical” is too restrictive; we will consider surface flux-powered storms outside the tropics. These could even include yet-to-be-discovered storms on extra-solar planets. Some larger dust devils may turn out to be driven by surface enthalpy fluxes and yet such vortices seem very far removed from the conventional definition of tropical cyclone. And one can always nitpick. What do we mean by “vortex”? There are other phenomena, such as convectively coupled equatorial waves, which might be driven by surface enthalpy fluxes, but these do not take the form of closed vortices (i.e. having closed contours of vorticity). What do we mean by “primarily”? Classical tropical cyclones often transition into baroclinic storms powered by pre-existing horizontal density gradients; at what point do they cease being “tropical cyclones”? We must recognize that there is a continuum between cyclones driven purely by surface enthalpy fluxes and those driven entirely by baroclinic conversion of background available potential energy. Bearing such caveats in mind, we forge on.

8.2. A note on terminology and metrics

Scientists interested in tropical cyclones confront a bewildering zoo of names, measurement conventions, and units owing to the different histories of the regions affected by these storms.

Distances and length scales are variously reported in conventional MKS units but also in nautical miles (1 nm = 1.852 km), statute miles (1.609 km) and, in the case of altitude, feet (1 ft = 0.3048 m). Velocities are often reported in nautical miles per hour, or “knots” (1 kt = 0.5144 ms^{-1}). Millibars (mb) are often used to quantify pressure (1 mb = 1 hectopascal or hPa). Throughout this text we will generally adhere to the conventional MKS system of units but will make exceptions where it seems desirable.

Tropical cyclones are classified according to their peak wind speeds. Unfortunately, even the definition of “wind speed” differs from one region to the next. U.S. agencies use a 1-minute

average, whereas elsewhere the average is taken over 10 minutes. ("Surface winds" usually refer to winds measured at the conventional altitude of 10 m.) Because boundary layer winds vary at high frequency, 1-minute peaks are larger than 10-minute peaks. In the absence of detailed information about boundary layer turbulence, a conversion factor of 0.88 is usually applied. In the definitions that follow, we use 1-minute averages.

We will use the word "intensity" synonymously with "wind speed", but central surface pressure is often used as a measure of storm intensity as well. Tropical cyclone "size" refers to the horizontal scale of the storm, and here several metrics are relevant. The most commonly used size metric is the radius of maximum winds (RMW); that is, the average distance from the storm center of the peak surface winds. It is also common to refer to the radius of gale force (17 ms^{-1} or 34 kt) winds, the radius of the outermost closed isobar (ROCI) of surface pressure, and the radius of vanishing wind (RVW); i.e., some measure of the radius of the outermost detectable influence of the tropical cyclone on surface winds. The diameter of the eye visible in satellite or radar imagery is sometimes recorded; this should not be confused with the radius of maximum winds.

There are three main intensity-based classifications of tropical cyclones[1]. The first and weakest is the *tropical depression*, defined to have winds less than 17 ms^{-1}. There is considerable ambiguity is identifying a system as a tropical depression, wrapped up in the problem of defining *genesis* (see Chapter 9). In particular, storms identified as tropical depressions may not even be tropical cyclones as we have defined them in section *a* above; that is, they may not at this stage be powered primarily by surface enthalpy fluxes. Indeed, tropical depression-strength cyclones occasionally develop over land and in these cases may not powered by surface fluxes (but see section c.viii on agukabams).

The term *tropical storm* is generally used to describe tropical cyclones with peak 1-minute winds between 17 and 32 ms^{-1}. Many different names are applied to storms with wind speeds higher than 32 ms^{-1}, and there are several classification schemes that further subdivide these more intense storms. For example, the term *hurricane* (derived from the various names, such as Hurácan and Hunraken, of the god of evil of pre-Columbian inhabitants of the Caribbean and Mexico) is used in the North (and South) Atlantic and eastern North Pacific, while *typhoon* (derived from the Chinese *jufeng* and/or the Greek earth demon *typhon*) is used in the western North Pacific. Sub-divisions of hurricane-intensity tropical cyclones include the Safir-Simpson scale, a 5-category subdivision used by the U.S. and several other nations[1].

For the purposes of this text, we use 1-minute average surface winds and MKS units to describe storm intensity and occasionally use the terms *tropical depression*, *tropical storm,* and *hurricane* as ways of classifying storms by intensity.

Well-developed tropical cyclones are highly coherent structures that can be tracked for long distances and time, so it is natural to give them names. In the North Atlantic region prior to 1950, significant storms were named informally, often after the places, ships, or even individuals they affected, or after the Saint's day on which their effects were felt. For example, a deadly hurricane that affected the Caribbean and Florida in 1928 is known in the continental U.S. today as the *Okeechobee Hurricane* (named after a large southern Florida lake whose

[1] A comprehensive summary of the classification schemes used by various government agencies worldwide may be found at https://en.wikipedia.org/wiki/Tropical_cyclone .

bordering towns were demolished by the storm) and as the *San Felipe Hurricane* in Puerto Rico. In Australia, Clement Wragge began naming storms in the late 19th century, ultimately using the names of unpopular politicians, a potentially limitless resource. Three storms were observed simultaneously during the 1950 North Atlantic hurricane season, causing much confusion and leading U.S. forecasters to begin using the Army/Navy phonetic alphabet (*Able, Baker, Charlie*) to identify individual tropical cyclones, replacing that in 1952 with the NATO phonetic alphabet (*Alpha, Bravo, Charlie*, etc.). From 1953 through 1978 North Atlantic tropical cyclones were given exclusively female names, after which alternating male and female names were applied. Today, all tropical cyclones of tropical storm strength or greater are named from pre-determined lists drawn up by one of eleven tropical cyclone warning centers, depending on the region affected.

8.3. Climatology

8.3.1. Frequency

Some 80 tropical cyclones form on our planet every year[2]. Since about 1980, by which time nearly all tropical cyclones were detected using satellites, there has been no significant trend in this number, and its year-to-year standard deviation is about 8.5, almost exactly the variability that would occur in a Poisson process (for which the standard deviation is the square root of the mean).

8.3.2. Geographic distribution

The tracks of all tropical cyclones in the historical record[3] from 1851 to 2010 are displayed in Figure 8.1. Figure 8.2 shows the number of tracks passing through each 3-degree latitude-longitude square each year, averaged over all the tropical cyclones in from 1980 to 2014.

The greatest concentration of tropical cyclones is in the western North Pacific region. These storms typically form south of 20° N, anywhere from the South China Sea eastward as far as the dateline, and move westward and northward. Those that do not strike land or otherwise dissipate often recurve northward and eastward, penetrating middle and high latitudes. Tropical cyclones form in the Bay of Bengal and in the Arabian Sea, mostly during the Boreal spring and fall. (Strong wind shear associated with the Asian summer monsoon suppresses formation during the summer.) The deadliest tropical cyclone in history struck East Pakistan (now Bangladesh) in November of 1970, killing between 300,000 and 500,000 people.

Another active region is the eastern North Pacific. Storms here typically develop off the west coast of Mexico and usually travel westward, rarely affecting land, but on occasion they recurve northward and eastward, striking the Mexican coast as far north as Baja California and may even reach southern California, bringing unusually heavy rains to that region. Some eastern Pacific tropical cyclones travel far enough west to affect the Hawaiian islands.

---

[2] These do not include some storms, such as polar lows, that develop under our extended definition of "tropical cyclone".

[3] See Appendix 1 for a detailed discussion of historical tropical cyclone data sets and for access to the historical data. These data sets do not include polar lows, medicanes, and other events not conventionally considered tropical cyclones. We hereafter refer to the data discussed in Appendix 1 as "the historical record".

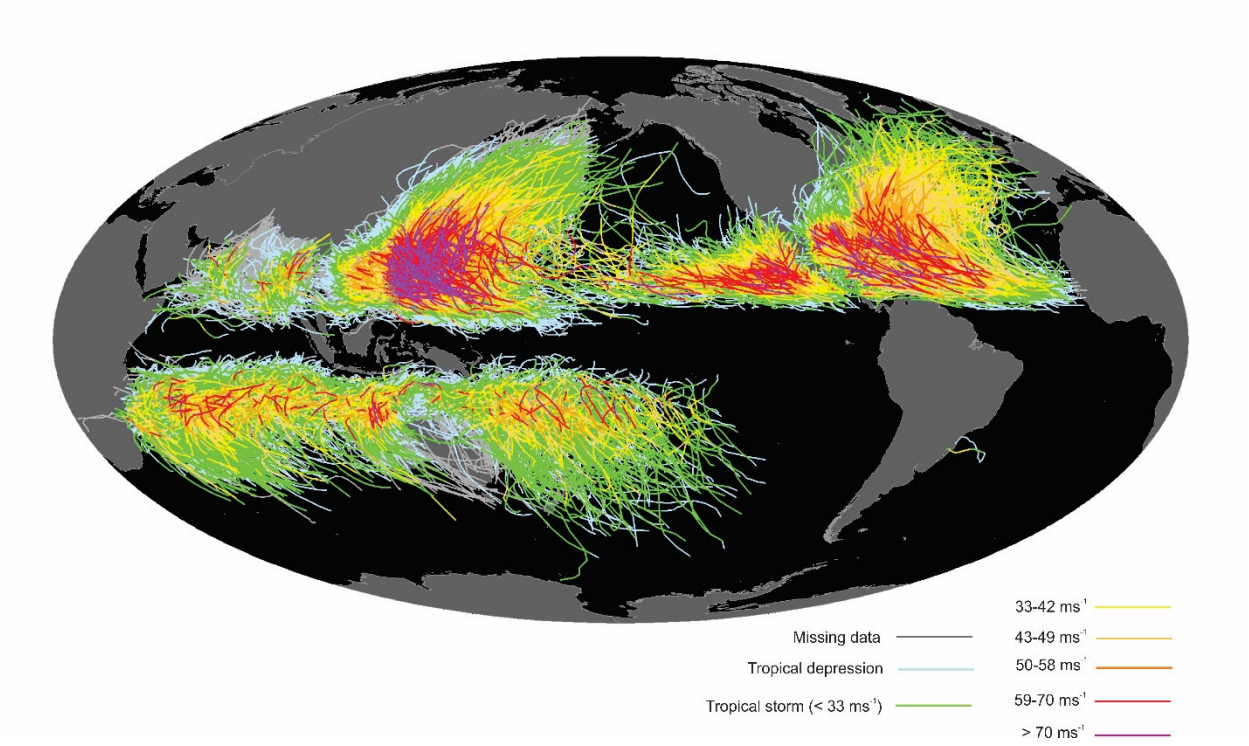

Figure 8.1: Tracks of all tropical cyclones in the historical record from 1851 to 2010. The tracks are colored according to the maximum wind at 10 m altitude, on the scale at lower right.

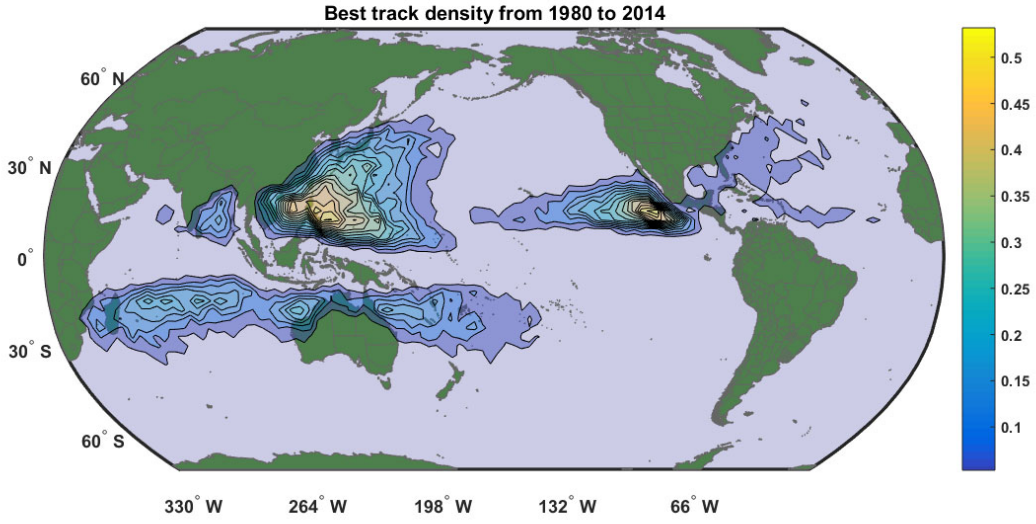

Figure 8.2: Number of historical tropical cyclone events per 3 x 3 degree latitude square per year averaged from 1980 to 2014. Color scale at right.

In the North Atlantic, tropical cyclones develop anywhere from the west African coast westward to the Caribbean and the Gulf of Mexico and as far north as 30° N off the coasts of the Carolinas. Once developed, they typically move westward and northward, and many eventually recurve northward and eastward, sometimes travelling far northward into the high latitudes of the North Atlantic. As shown in Figure 8.2, the density of tracks in the North Atlantic is low compared to other cyclone-prone regions, and only about 12% of all tropical cyclones develop there. Yet much of the literature focuses on North Atlantic storms because, on average, they are far better observed than storms in other regions, thanks to a vigorous program of aircraft reconnaissance dating back to the mid 1940s. There is much more media coverage of North Atlantic storms because their destructiveness is far out of proportion to their number, owing to the very high concentration of wealth along the U.S. east and Gulf coasts, coupled with poor risk management policies.

There are no tropical cyclones within a few degrees latitude of the equator, because long-lived cyclonic vortices require a non-zero Coriolis parameter (the projection onto the local vertical of twice the planetary angular rotation vector.) There is an active belt of tropical cyclones in the southern hemisphere, stretching from Mozambique across Madagascar and the Southern Indian Ocean, northern Australia, and into the South Pacific as far east as French Polynesia.

In the historical record from 1851 to 2015 there has been only one hurricane-strength tropical cyclone in the South Atlantic, Hurricane *Catarina* of March, 2004; this event did considerable damage in Brazil. It is possible that a few events occurred in the South Atlantic between 1851 and the dawn of the satellite era and were not detected by ships or land-based observations.

8.3.3. Life Cycle

Most, if not all, tropical cyclones originate in preexisting disturbances of largely independent origins. (At least, that is the reigning dogma in tropical meteorology. We shall see in Chapter 9 that tropical cyclones can develop spontaneously in computational models under certain circumstances.) For this reason, it is difficult, on a purely phenomenological basis, to decide when a tropical cyclone has formed. While there is no generally accepted set of criteria for when a tropical cyclone has developed, most operational forecast centers will declare that a tropical depression has formed based on the existence of a closed surface wind circulation around a well-defined center, assuming that the system is otherwise broadly consistent with expectations based on structure and climatology.

Figure 8.3 shows the origin points of all tropical cyclones in the historical record (Appendix 1) between 1980 and 2014. There are three main genesis regions: the North Atlantic including the Caribbean and the Gulf of Mexico, extending westward across Mexico to the eastern tropical North Pacific. A second region, not altogether separated from the first, spans from the central North Pacific across the far western North Pacific and southeast Asia to the Bay of Bengal and the Arabian Sea. In the Southern Hemisphere, tropical cyclones originate from just east of French Polynesia westward across the South Pacific, spanning the region around northern Australia, including the Coral and Timor Seas and the Gulf of Carpentaria, and across the whole of the South Indian Ocean across Madagascar to Mozambique, southern Tanzania, and the northeast coast of South Africa.

As mentioned above, tropical cyclones do not develop near the equator because they require a sufficiently large absolute value of the Coriolis parameter (the projection of the twice the angular velocity vector of the earth's rotation onto the local vertical). One exceptional storm was Cyclone

Agni that developed at around 1.5° N in the Indian Ocean in November of 2004, traveling as far south as 0.7° N. Close inspection of Figure 8.3 shows a tropical cyclone developing near Nova Scotia. This was Tropical Storm *Grace* of 2009, which developed near 45° N. This was an example of an extratropical cyclone that eventually travelled far enough south to become a tropical cyclone.

As we will see in Chapter 4, tropical cyclones develop where the thermodynamic potential is high and where the absolute value of the Coriolis parameter is sufficiently large. We will examine the physics of genesis in Chapter 9.

Once formed, tropical cyclones will continue to develop unless and until environmental conditions become adverse. An obvious case is when they travel over land, losing the upper ocean reservoir of heat that sustains them. (But see the section on agukabams later in this chapter.) They may also travel into regions whose thermodynamic potential (Chapter 4) is insufficient, causing them to decay and eventually dissipate. Vertical shear of the horizontal wind is highly deleterious to tropical cyclones (Chapter 8) and may lead to dissipation even under otherwise very favorable conditions. Finally, tropical cyclones may undergo a transition to baroclinic systems, a process known as *extratropical transition* (Chapter 8), and they may even re-intensify in their new incarnations, generally becoming physically larger and sometimes very destructive.

Under idealized conditions in numerical simulations, tropical cyclones may persist indefinitely (see Chapter 9). But in the real world, only a few tropical cyclones intensify right up to their thermodynamic limiting intensity (Chapter 4). The vast majority lead lives of quiet desperation, struggling against environmental adversity, occasionally triumphing but finally succumbing to any of a variety of fatal influences.

Figure 8.4 shows a histogram of the lifetimes (times between first and last points in the historical track database) of all tropical cyclone globally between 1980 and 2014. The average storm lifetime is almost exactly one week, and the median lifetime is 6.5 days. The longest lasting tropical cyclone on record is generally taken to be Typhoon *John,* which formed in the eastern North Pacific on 11 August 1994 and dissipated 31 days later on September 10th, after traveling a remarkable 13,280 km path westward and then northward across the North Pacific. But according to the U.S. Joint Typhoon Warning Center, Cyclone *Pancho-Helinda*[4] of 1997 lasted more than 32 days as it traversed virtually the entire South Indian Ocean.

The last track point in historical databases is just as arbitrary as the first. In most cases, tropical cyclones are considered to have dissipated when their peak surface winds drop below some threshold, typically 25 knots. But the track may end when the storm is considered to have transitioned to a primarily baroclinic system, even though its maximum surface winds may be well in excess of the usual threshold.

Figure 8.5 shows the last track points of all tropical cyclones in the historical record from 1980 to 2014. Termination points are as far poleward as the Labrador Sea and as far inland as Ontario and central Australia.

[4] The storm's initial name was *Pancho* but it was renamed *Helinda* when it passed into the southwestern Indian Ocean.

8.3.4. Seasonality

Tropical cyclones form preferably in the summer and early fall, as shown in Figure 8.6. An exception to this rule is the North Indian Ocean, which exhibits two peaks, one in May and the other in October and November. As we will discuss in Chapter 8, tropical cyclones are strongly suppressed by vertical shear of the horizontal wind, which becomes large during the Asian summer monsoon.

8.3.5. Intensity

Analysis of the climatology of tropical cyclones is compromised by the relatively poor quality of measurements of storm intensity. As described in Appendix 1, reliable estimates based on aircraft and aircraft-deployed dropsondes are only available in the North Atlantic from roughly the late 1950s to the present, and in the western North Pacific from the late 1950s to 1987, when aircraft reconnaissance was discontinued there. Aircraft reconnaissance extends back to about 1945 in both basins, but quantitative intensity estimates were based on central pressure, if dropsonde measurements were available, or extrapolation of flight level pressure data to the surface using flight level temperature and a standard temperature profile (such as a moist adiabat). Direct wind speed estimates were made by visual inspection of the sea surface, but these necessarily have a strong subjective component. By the late 1950s or early 1960s, forward-scanning Doppler radars were installed on some aircraft, allowing for a quantitative estimate of the aircraft's ground speed. By around 1968, implementation of inertial navigation systems on reconnaissance aircraft further increased the accuracy of flight level winds. Beginning in about 1980, earth-orbiting satellites detected most tropical cyclones around the globe, and methods were developed to estimate storm intensity from satellite-based measurements.

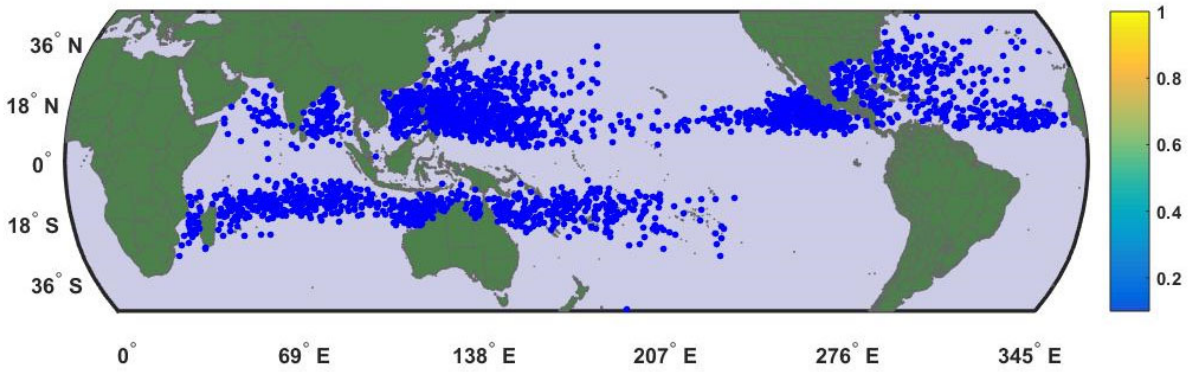

Figure 8.3: Points of origin of all tropical cyclones in the historical record between 1980 and 2014. This does not include polar lows, medicanes, or agukabams.

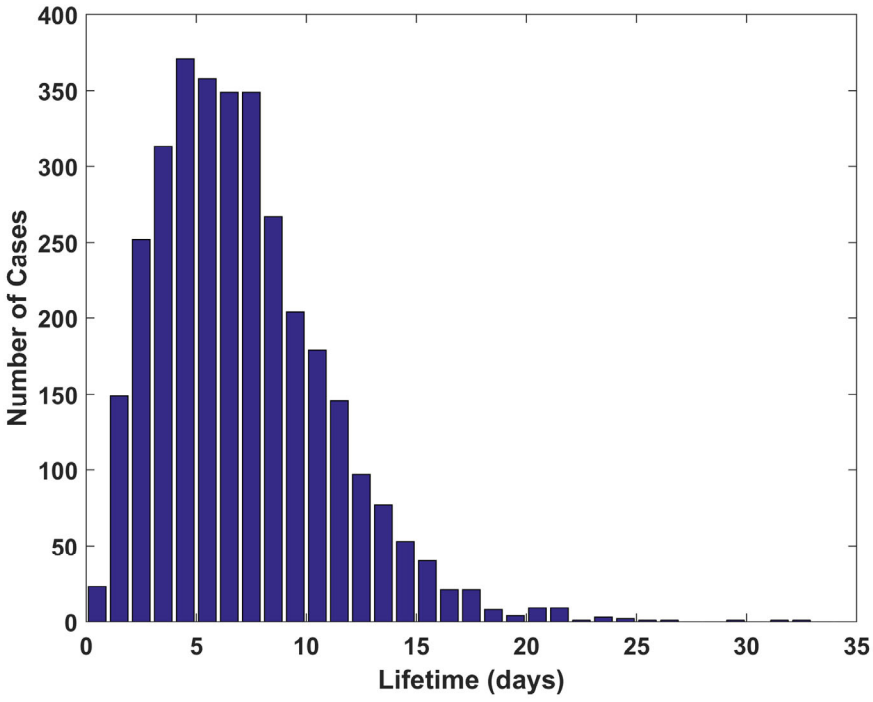

Figure 8.4: Histogram of the lifetimes of tropical cyclones globally, from 1980-2014. The number of cases are binned into intervals of 1 day.

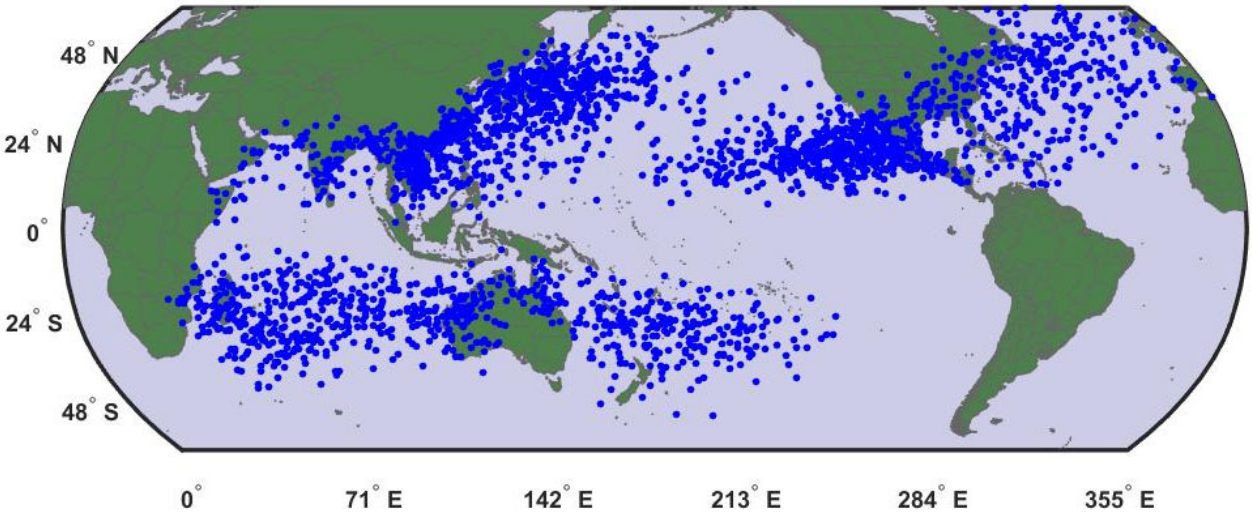

Figure 8.5: Termination points of all tropical cyclones in the historical record from 1980 to 2014. This does not include polar lows or medicanes, though some agukabams may be included.

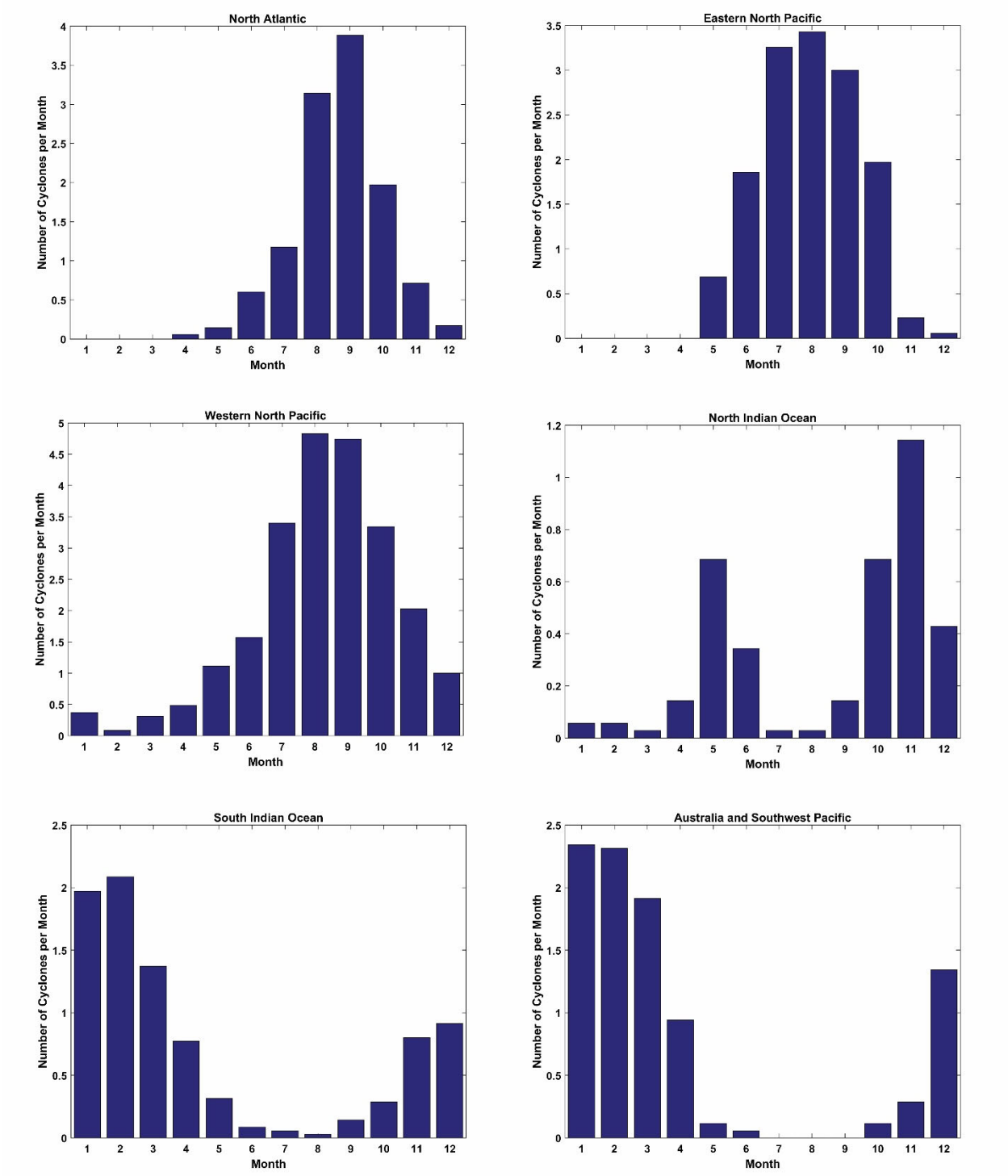

Figure 8.6: Number of tropical cyclones per month, averaged over the period 1980-2014, in six ocean basins. From left-to-right and top-to-bottom: North Atlantic, eastern North Pacific, western North Pacific, north Indian, south Indian, and Australia and the southwestern Pacific.

One useful measure is the maximum surface wind estimated for each storm during its lifetime. This quantity is known as its *Lifetime Maximum Intensity (LMI)*. Figure 8.7 shows the probability densities of LMI for tropical cyclones in the North Atlantic and western North Pacific regions over the period 1945-1987, during which there was aircraft surveillance of at least some of the events.

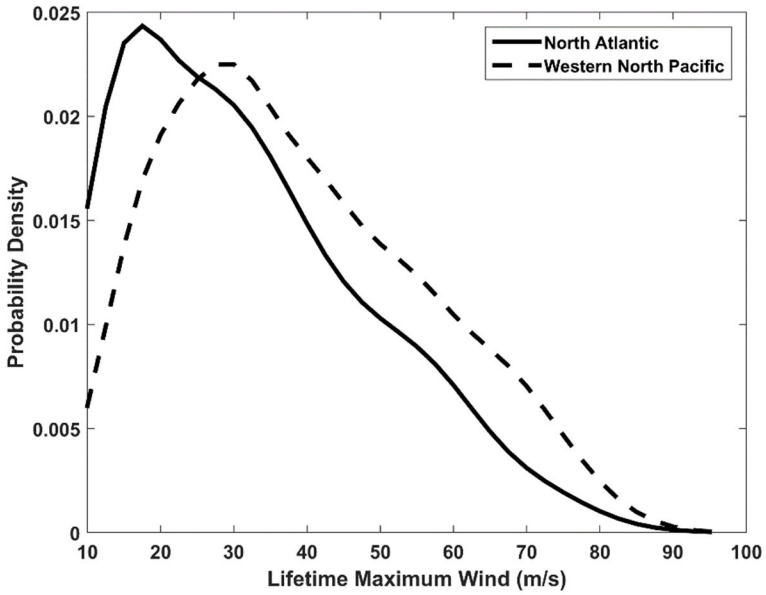

Figure 8.7: Probability densities of lifetime maximum intensities (LMIs) of tropical cyclones in the North Atlantic (solid) and western North Pacific (dashed) from 1945 to 1987. The probabilities are calculated on intervals of 2.5 ms^{-1}.

For storms of hurricane strength (> 32 ms^{-1}), the probability density decreases nearly linearly with LMI. Note that the probability distribution is bounded; there are no recorded cases of wind speeds in excess of 100 ms^{-1}. The world record tropical cyclone wind speed of 95 ms^{-1} was set by eastern North Pacific Hurricane *Patricia* of 2015.

Figure 8.8 shows the probability densities of tropical cyclones in the eastern and western North Pacific in the period 1988-2014, during which almost all the intensity estimates were made using satellite-based techniques (Appendix 1). In contrast to the probabilities during the aircraft reconnaissance era (Figure 8.7), the distributions are noticeably bimodal. As of this writing, it is not known whether this difference is owing to climate change between the earlier and later periods or to differences between aircraft-based and satellite-based intensity inferences.

A map of the average annual maximum tropical cyclone surface wind over each 3 degree latitude-longitude square is shown in Figure 8.9. The most intense storms are in the far eastern and far western North Pacific.

Any serious student of tropical cyclone intensity must be aware of the substantial inhomogeneities that plague the historical tropical cyclone record, brought about by different techniques for estimating intensity and evolving standards and techniques. Historical intensity data should not be accepted at face value. We shall have more to say about climatological tropical cyclone intensity in Chapter 4.

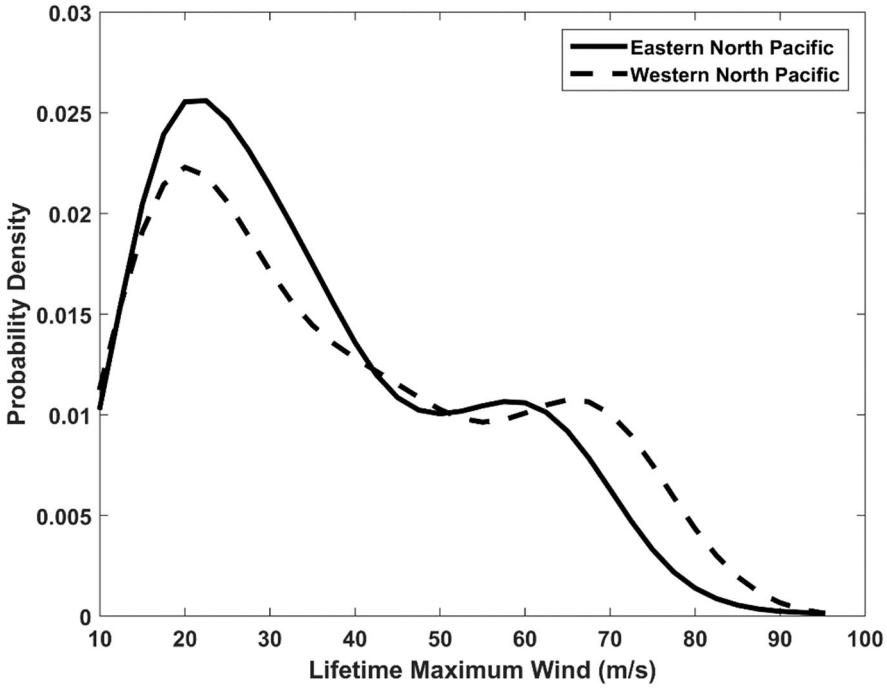

Figure 8.8: Probability densities of lifetime maximum intensities (LMIs) of tropical cyclones in the eastern (solid) and western (dashed) North Pacific from 1988 to 2014. The probabilities are calculated on intervals of 2.5 ms^{-1}.

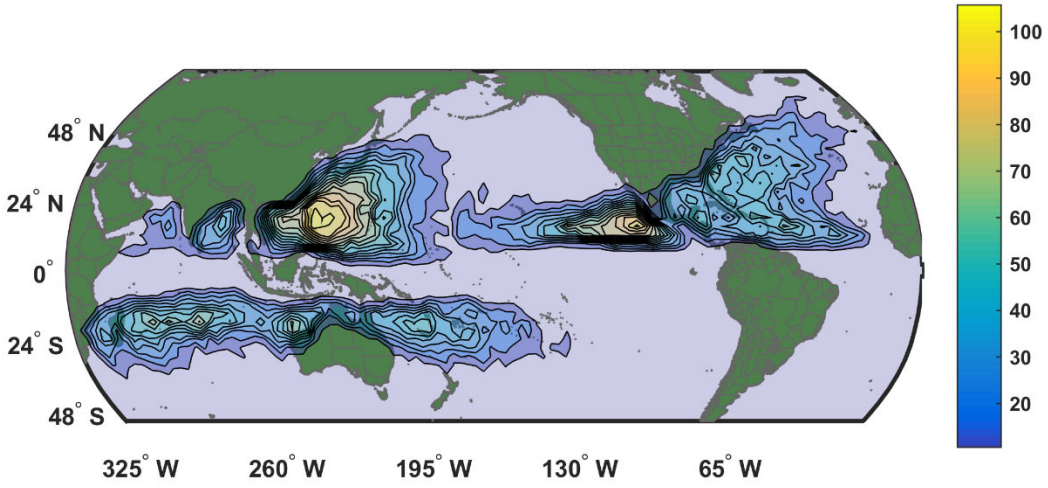

Figure 8.9: Annual maximum tropical cyclone wind speed (ms^{-1}) in each 3 x 3 degree latitude square, averaged over the period 1980-2014.

8.3.6. Size

Tropical cyclone diameters span a wide range. Atlantic tropical storm *Marco* of 2008 had gale force (17 ms^{-1}) winds extending outward to only about 18 km; its radius of vanishing winds was likely less than 40 km. Yet the eye of Typhoon *Carmen* of 1960 was measured by radar to have a radius of 160 km, so that four entire *Marcos* could fit within *Carmen's* eye.

Climatologies of tropical cyclone size metrics are compromised by a comparative dearth of recorded observations. Historical data for the North Atlantic and eastern North Pacific now contains information about the radii of gale force (17 ms^{-1}), 25 ms^{-1} and hurricane force (33 ms^{-1}) winds going back to 2004, but this information is not available for every storm at every observation time. Similarly, size information is available in historical tropical cyclone data provided by the U.S. Joint Typhoon Warning Center (JTWC) going back to 2001. (See Appendix 1 for a description of and access to these data sets.)

One measure of size is the radius of maximum winds (RMW), which refers to the azimuthally averaged radius at which surface winds reach their peak values. (As discussed later in this chapter, there can be secondary and even tertiary wind maxima at various radii outward or inward from the primary RMW.) The RMW can vary greatly within the lifetime of an individual storm, and from one storm to the next; for a given storm, it generally contracts as the storm intensifies, but secondary eyewalls can form at greater radii and contract inward, choking the original eyewall and replacing it at a greater radius (see section *c*). As this metric is rather sparsely reported in standard historical tropical cyclone data sets, we here use global satellite-based estimates over the period 1983-2005, as reported by Kossin et al. (2007). Figure 8.10 shows the probability density of the RMW from this data set, which contains 11,937 individual fixes. The mean RMW is around 65 km, and most storms have RMWs between 20 and 100 km.

Another useful and interesting size metric is the radius of vanishing wind (RVW), defined as azimuthally averaged distance from the storm center at which there is no detectable influence of the tropical cyclone on surface winds. This metric is entirely absent from conventional historical data sets because it is very difficult to determine from aircraft data or from satellite visible or infrared imagery. One way to estimate the RVW is to fit a theoretically derived outer wind profile to observations at intermediate radii and use that to extrapolate out to the RVW (Dean et al., 2009). An even better method is to take advantage of winds determined from satellite-based sea surface scatterometry. A scatterometer send pulses of microwave radiation downward at an angle to the sea surface and measures the power of the back-scattered radiation. The pulses have a wavelength such that they are Bragg-scattered from capillary-gravity waves on the sea surface; these are usually nearly in equilibrium with the surface wind stress. By measuring the backscattered power from several different viewing angles as the satellite orbits, the orientation of the waves can be determined, giving the direction of the wind stress; the magnitude of the backscattered radiation is proportional to the amplitude of the stress. Empirical and/or theoretical relationships are used to deduce standard 1-minute winds at 10 m altitude form the surface stress. An example of a surface wind field associated with a western North Pacific typhoon is shown in Figure 8.11. Heavy rain also strongly backscatters scatterometer pulses, introducing errors, and so the technique does not work well in the inner core regions of tropical cyclones, where heavy rain is the norm. But the technique works well in the outer regions, which are usually free of heavy rain.

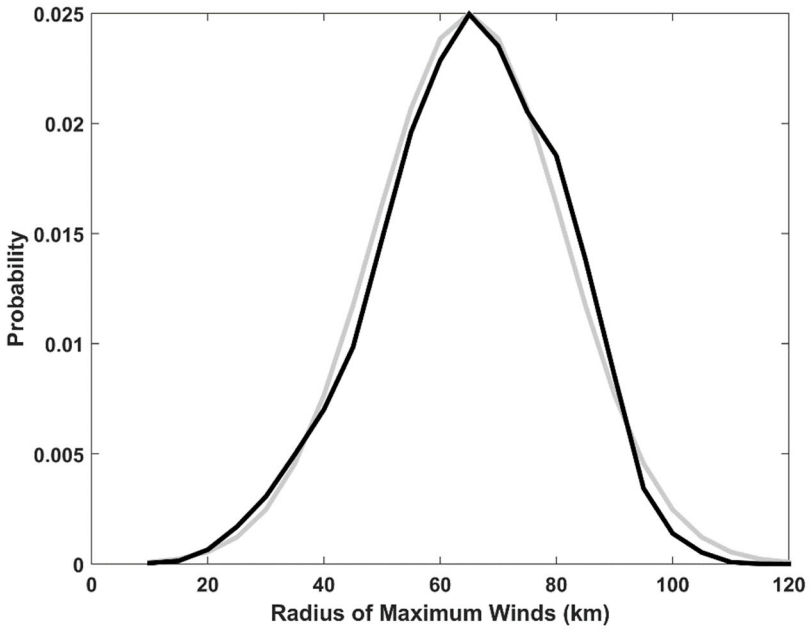

Figure 8.10: Probability density (black curve) of the radii of maximum winds (km) estimated from satellite infrared imagery by Kossin et al. (2007). The probabilities are binned in 5 km intervals of RMW. The gray curve is a best fit Gaussian distribution.

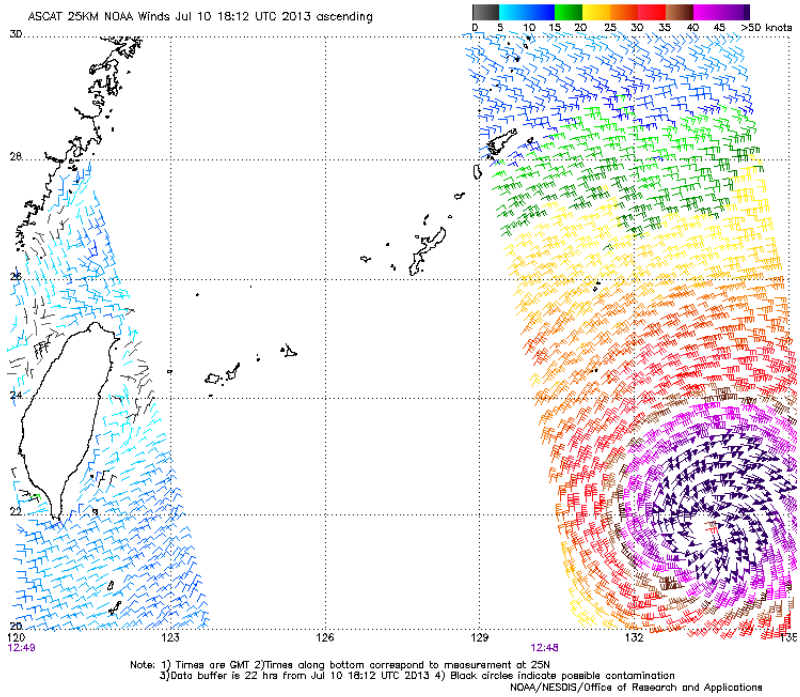

Figure 8.11: Surface winds associated with Typhoon Soulik on July 10th, 2013 determined from by Eumetsat's ASCAT (Advanced Scatterometer) instrument on board the Metop-A satellite. The barbs point into the wind, and the colors indicate the wind speeds according to the scale at upper right.

Here we rely on the work of Chavas and Emanuel (2010), who used QuickSCAT scatterometer data from 1999 to 2008 to determine the radius at which the azimuthally averaged wind falls to 12 ms^{-1}. They then used the same outer wind model as employed in Dean et al. (2009) to estimate the RVW. They found that the frequency distribution of the RVW is very nearly lognormal (Figure 8.12) with a global median corresponding to an RVW of 423 km. They also found that, in contrast to the RMW, the RVW typically varies little over the life of a given storm but can vary greatly from one storm to the next.

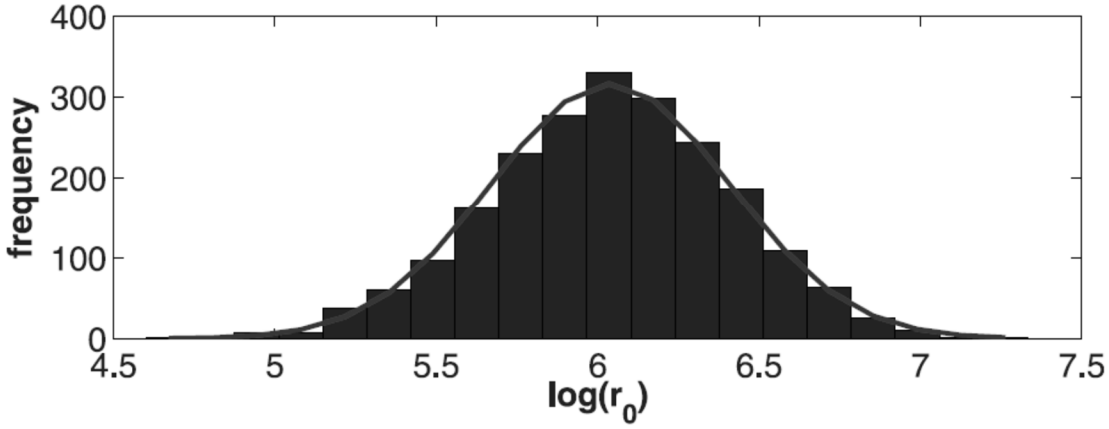

Figure 8.12: Frequency distribution of the natural logarithm of the radius (km) of vanishing wind (RVW, here indicated as r_0) from 2154 scatterometer observations of tropical cyclones as reported in Chavas and Emanuel (2010). The frequencies were calculated in bins of width 0.1 in the natural logarithm of the RVW.

8.3.7. Rain

Tropical cyclones produce extremely heavy rain. The worlds' record rainfalls at 12, 24, 72, and 96 hours were all caused by the interaction of tropical cyclones with the island of La Réunion in the South Indian Ocean. But rain is difficult to measure, because the correlation lengths scales of precipitation are small, particularly in convective events, and sampling by limited arrays of rain gauges is thus highly problematic. At sea, where tropical cyclones spend most of their lives, there are no gauges aside from those on the odd island station. Land-based radars, which measure the power of backscattered microwave radiation, are useful for detecting tropical cyclone rainfall over land and coastal waters, though deducing actual rainfall rates from radar reflectivity is not straightforward and subject to some uncertainty.

From late November 1997, to mid April, 2015, the National Aeronautics and Space Administration (NASA) and the Japan Aerospace Exploration Agency conducted the Tropical Rainfall Measuring Mission (TRMM) to quantify precipitation in the tropics. It carried a microwave precipitation radar, allowing active measurement of precipitation from space. Figure 8.13 shows a global climatology of tropical precipitation over the period 1998-2006 as well as rainfall attributed to tropical cyclones. This was made by combining TRMM precipitation radar measurements with conventional passive infrared from a variety of satellites (Huffman and co-authors, 2007). These measurements show that tropical cyclone contribute roughly 7% of the total precipitation in the tropics, though there are a few locations in which they contribute greater than half the total. The general pattern of tropical cyclone rainfall resembles that of tropical cyclone tracks (Figure 8.2), as one might expect.

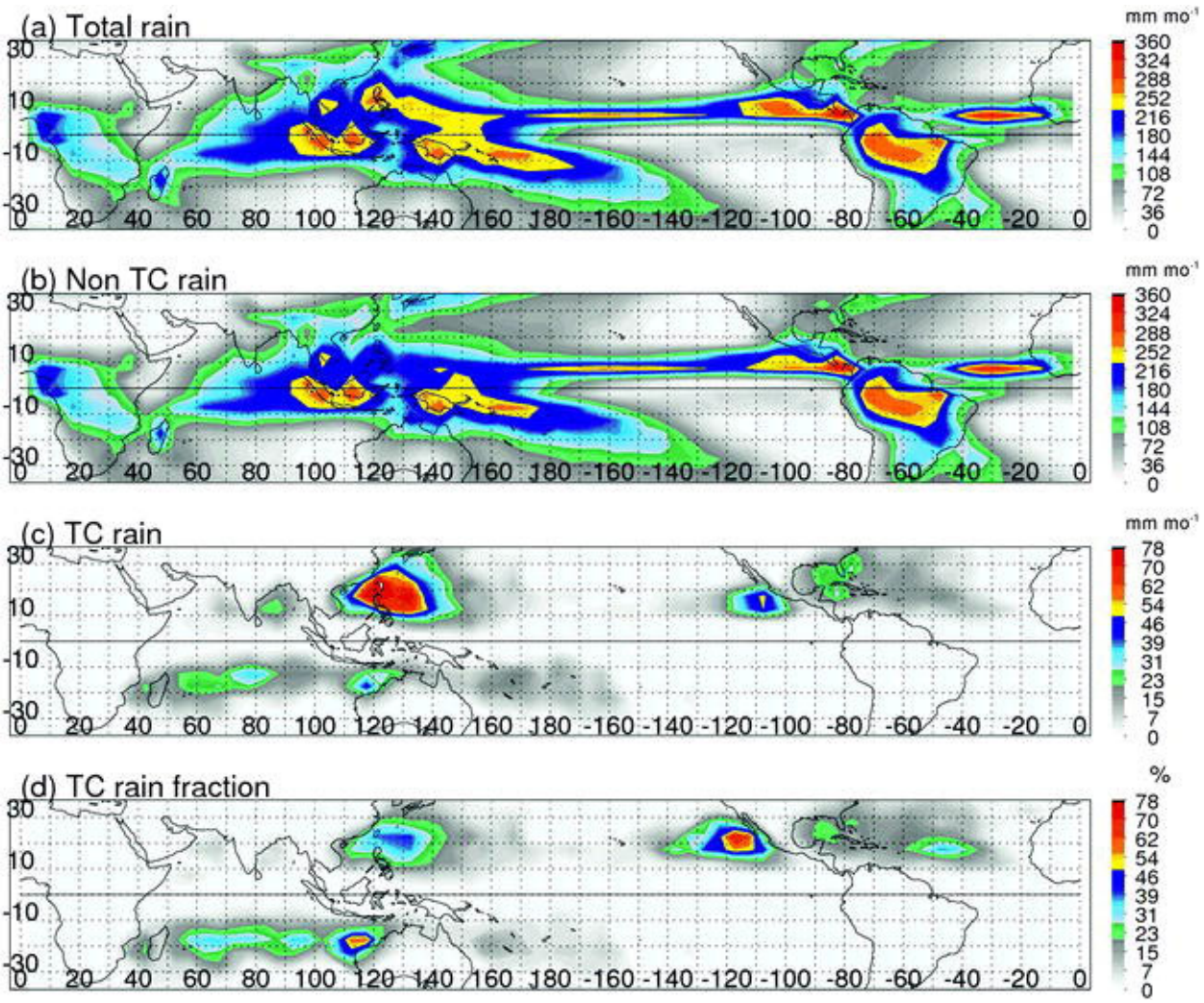

Figure 8.13: Tropical climatology of precipitation (mm per month) from a combination of TRMM precipitation radar and conventional infrared measurements from other satellites over the period 1998-2006. Panel (a) shows the total rainfall, while the non-tropical cyclone, tropical cyclone, and fraction (%) of tropical cyclone rainfall are shown in panels b,c, and d. From Jiang and Zipser (2010).

Although tropical cyclones do not dominate tropical mean precipitation, they do contribute disproportionately to rainfall extremes on time scales of several days and are a major source of freshwater flooding in many tropical cyclone-prone locations.

8.3.8. Polar Lows, Medicanes, and Agukabams

Thermodynamic conditions over warm tropical oceans are nearly always conducive to the development of tropical cyclones, as demonstrated in Chapter 4. The strong thermodynamic disequilibrium between the atmosphere and the surface, necessary to sustain tropical cyclones, is usually absent outside the tropics, but there are occasions when deep masses of cold air move over relatively warm water and thermodynamic conditions become temporarily favorable for flux-driven vortices to develop.

Wintertime outbreaks of deep, cold air over relatively warm water occur regularly in the far North Atlantic east of Greenland and over the Norwegian and Barents Seas, and in the North Pacific region including the Sea of Japan. Polar lows have also been detected in the Southern Ocean

near Antarctica. The more severe polar lows are usually accompanied by deep, cut-off cyclones in the middle and upper troposphere, which provide low-shear environments near their centers. The strong thermodynamic disequilibrium between the deep, cold arctic air and the relatively warm sea surface in these regions (where they are free of sea ice) provide favorable conditions for tropical cyclone-like development. Since these regions can be highly baroclinic as well, it is not always easy to distinguish surface flux-driven cyclones from conventional baroclinic cyclones and indeed there is likely a continuum between these two end member cyclone types. In models and to some extent in reanalysis data sets, it is possible to quantify baroclinic and surface-flux driven energy sources, but the quantity of observations in these regions is generally insufficient for quantitative analysis and inferences about the physical mechanism are based mostly on the appearance of the vortices in satellite imagery and on assessment of the thermodynamic potential for flux-driven cyclones from nearby soundings, if they exist, or operational analyses or reanalyses.

Figure 8.14a shows the density of polar lows identified in numerical simulations made using a regional model driven by boundary and initial conditions provided by a reanalysis data set (Zhan and von Storch, 2008). The polar lows were identified objectively using criteria based on the sea level pressure perturbation and the difference between the ocean temperature and the temperature at 500 hPa, the latter insuring that the thermodynamic environment could support flux-driven vortices. Similarly, Figure 8.14b shows the origin points and tracks of polar lows over the Sea of Japan identified in a high resolution reanalysis (Yanase and co-authors, 2016). In both case, the activity peaks in mid-winter, when the air-sea temperature contrast is greatest during cold-air outbreaks.

A phenomenon similar to polar lows has been observed over the Mediterranean Sea during the colder months. These are relatively rare, with an annual probability of around 1.5, and they develop under circumstances nearly identical to those of conventional polar lows…usually under deep, cut-off cyclone aloft. As with polar lows, the enhanced air-sea temperature contrast and low wind shear near the center of such cut-off cyclones provides a conducive environment for flux-driven vortices. Likewise, medicanes are most common during the winter months when the contrast between the air temperature in cold air outbreaks and the sea surface temperature is greatest. The incidence of medicanes is small enough that climatologies made over the course of the satellite era tend to be noisy (Cavicchia et al., 2014), and so in Figure 8.15 we present a climatology produced by downscaling ERA-40 reanalyses over the period 1981-2000 (Romero and Emanuel, 2013). Medicanes favor the central Mediterranean but can occur throughout the region and in the Black Sea as well.

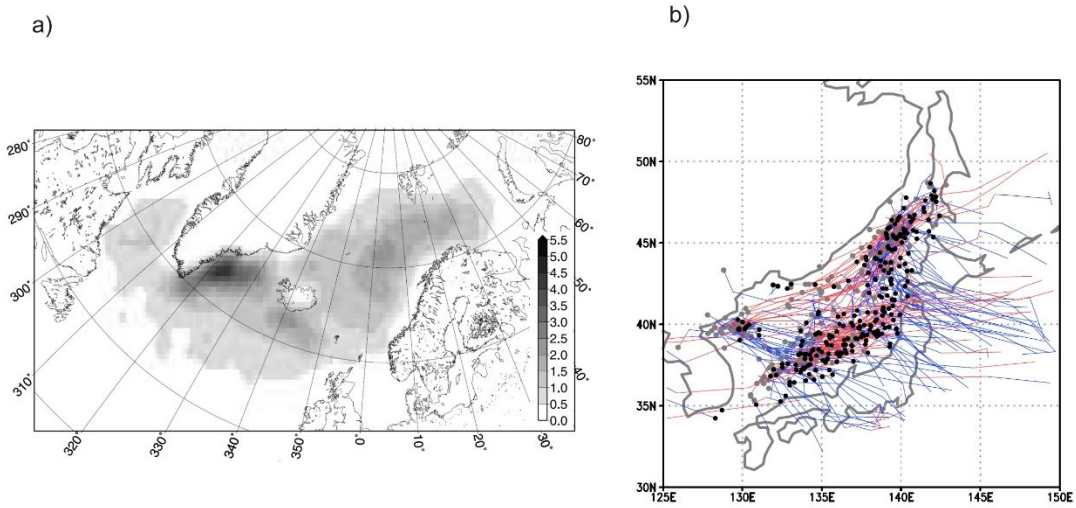

Figure 8.14:a) Polar lows per 250 km^2 in the North Atlantic, downscaled from NCAR/NCEP reanalyses over the period 1948-2006 (Zhan and von Storch, 2008). b) Origin points and tracks of polar lows over the Sea of Japan identified in JRA-55 reanalyses over the period 1979-2015 (Yanase and co-authors, 2016).

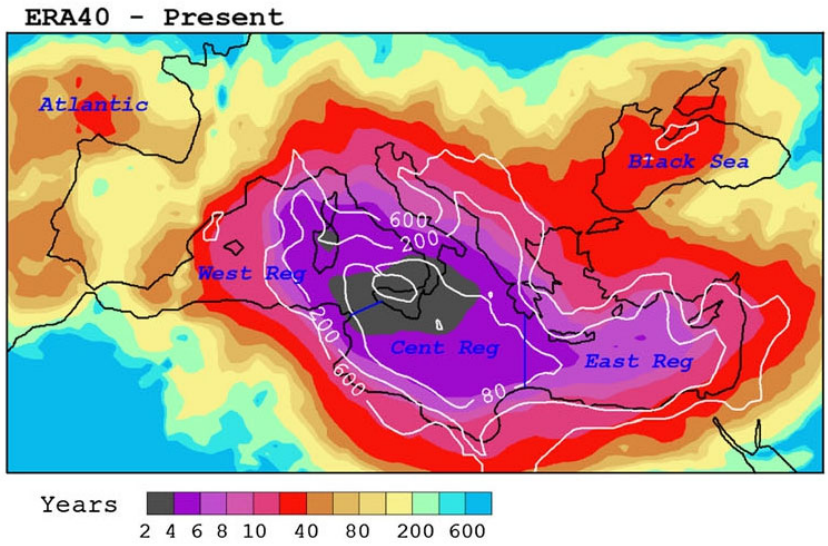

Figure 8.15: Return periods for the present climate of medicane surface winds above 34 kt (color) and 60 kt (white contours, for the values shown in the color scale). From Romero and Emanuel (2013).

Even rarer than medicanes are *agukabams* (a word constructed from the Australian aboriginal Ayapathu word roots “agu,” meaning land, and “kabam,” meaning storm), also known as *landphoons*. These are tropical cyclone-like storms that develop over land in the absence of appreciable baroclinic forcing (as happens with extratropical transition) and may be powered by surface enthalpy fluxes made possible when hot sand is wetted by precursor rains, temporarily increasing the thermal conductivity of the soil to the point that appreciable heat can escape to the atmosphere (Emanuel et al., 2008). This appears to happen most frequently over the deserts of northern Australia, where relatively dark soils can absorb much sunlight in summer. It is possible that some cases of inland intensification elsewhere are also owing to unusually large heat fluxes from the soil; there is some indication that Tropical Storm Erin of 2007 re-intensified over Oklahoma because of enhanced surface enthalpy fluxes (Evans et al., 2011). As of this writing, no formal climatology of agukabams has been published. Figure 8.16 shows a TRMM image of informally named Agukabam Abigail in March of 2001. The storm had been over land for almost 4 days when this image was made, and yet it still has the structure of a developed tropical cyclone (Emanuel et al., 2008). Figure 8.17 shows the track and evolution of an agukabam in northern Australia in January of 2006 (Tang et al., 2016). Observations of the storm make it clear that it intensified while over land.

We will have more to say about polar lows, medicanes, and agukabams in Chapter 8.

8.4. Structure

8.4.1: Overview

Tropical cyclones are complex bounded vortices, with cyclonic flow at low levels decaying with altitude and becoming anticyclonic near their tops, which are generally close to the tropopause. A broad overview of the structure of clouds and airflow in a fully developed northern hemisphere tropical cyclone is displayed in Figure 8.18. A central core, called the *eye*, generally free of clouds and becoming broader with altitude, is surrounded by an outward slopping *eyewall*, a dense concentration of cumulonimbus convection underneath which the strongest winds and heaviest rains of the storm are found. Outside the eyewall, deep convection is organized into bands which may take the form of *concentric eyewalls* (also referred to as *secondary eyewalls*) – nearly annular bands of deep precipitating cumulonimbi more or less centered at the storm center – or *spiral rainbands*, which are clearly evident in satellite and radar imagery. For example, Figure 8.19 is a satellite image of Hurricane *Ivan* of 2004 as it approached the Gulf Coast of the U.S. in 2004. Several nice spiral bands are visible outside the primary eyewall cloud, and the eye itself is prominent. Figure 8.20 has been constructed from reflectivity data from the ELDORA (ELectra DOppler RAdar) mounted on the Naval Research Laboratory Lockheed P-3 Orion aircraft. This is an X-band radar, emitting pulses of radiation of wavelength 8.2 cm that backscatter from precipitation particles. The reflectivity, corrected for distance from the radar, is a rough measure of the concentration of rain. The eye, indicated by white (no radar returns), is at the center of this image and is surrounded by an almost-closed reflectivity maximum (the eyewall). Outside the primary eyewall is a pronounced reflectivity minimum, sometimes referred to as the *moat*. In this particular case, a very pronounced secondary eyewall is present outside the moat, made visible by a nearly closed maximum of radar reflectivity. Spiral bands of radar reflectivity begin on the north and south sides of the secondary eyewall and spiral outward from there.

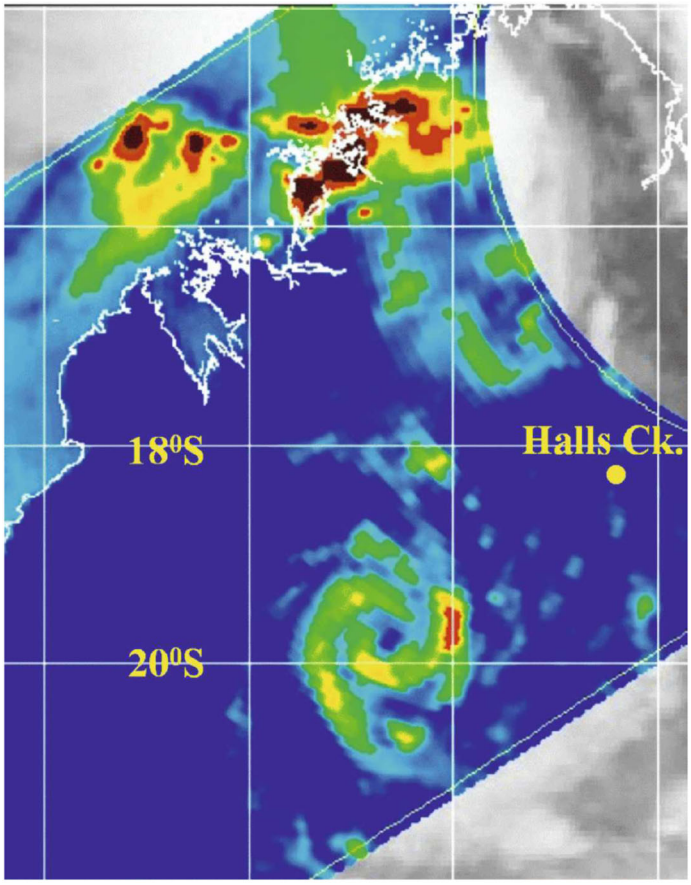

Figure 8.16: A Tropical Rainfall Measuring Mission (TRMM) 85-GHz (horizontally polarized) microwave image of Agukabam Abigail in northwestern Australia, at 1903 UTC 2 March 2001. From Emanuel et al. (2008).

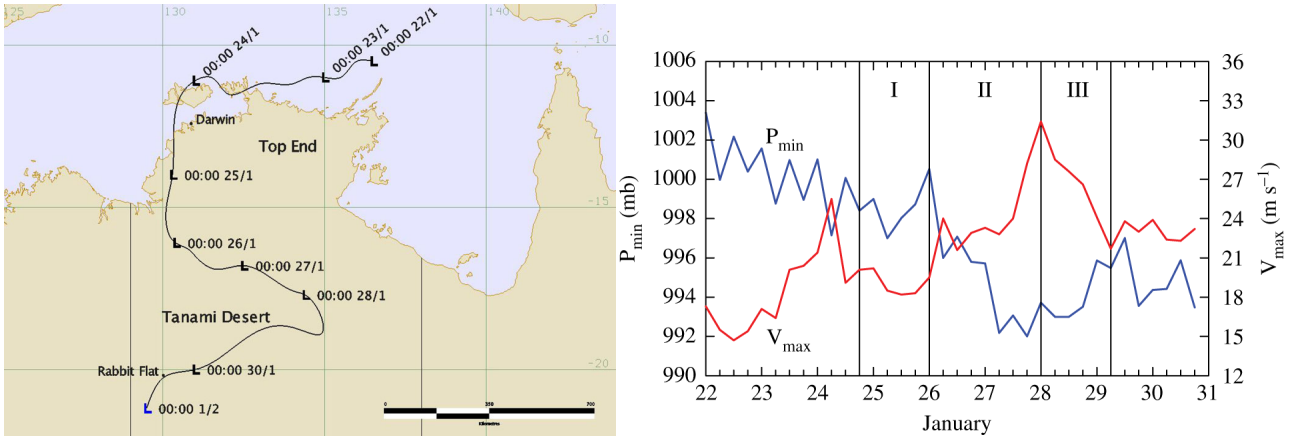

(a) (b)

Figure 8.17: a) Track through northern Australia of agukbam of January, 2006. b) Time series of the minimum sea-level pressure, P_{min}, and maximum horizontal total wind speed at the height of 850 mb, V_{max}, from European Center for Medium Range Forecasts analyses. From Tang et al. (2016).

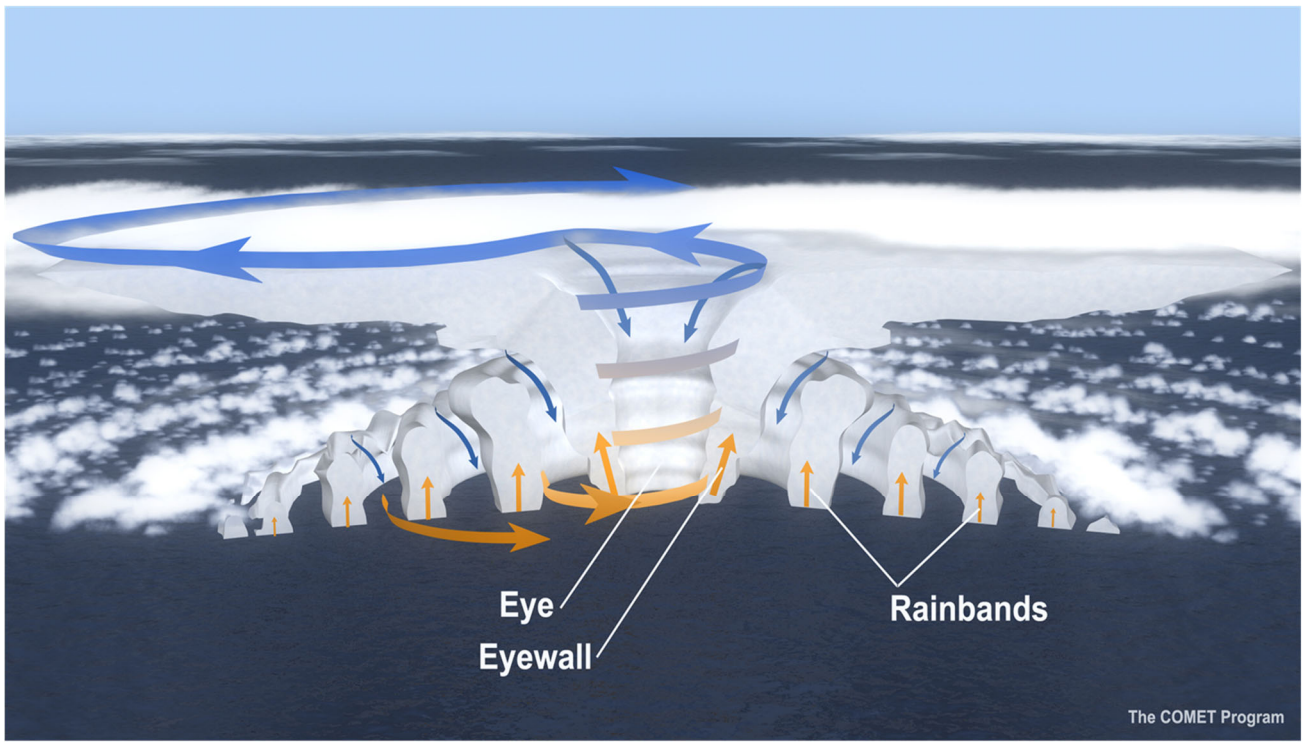

Figure 8.18: Overview of clouds and airflow in a northern hemisphere tropical cyclone. The diagram represents a cross section of roughly 500 km in diameter and 18 km in altitude.

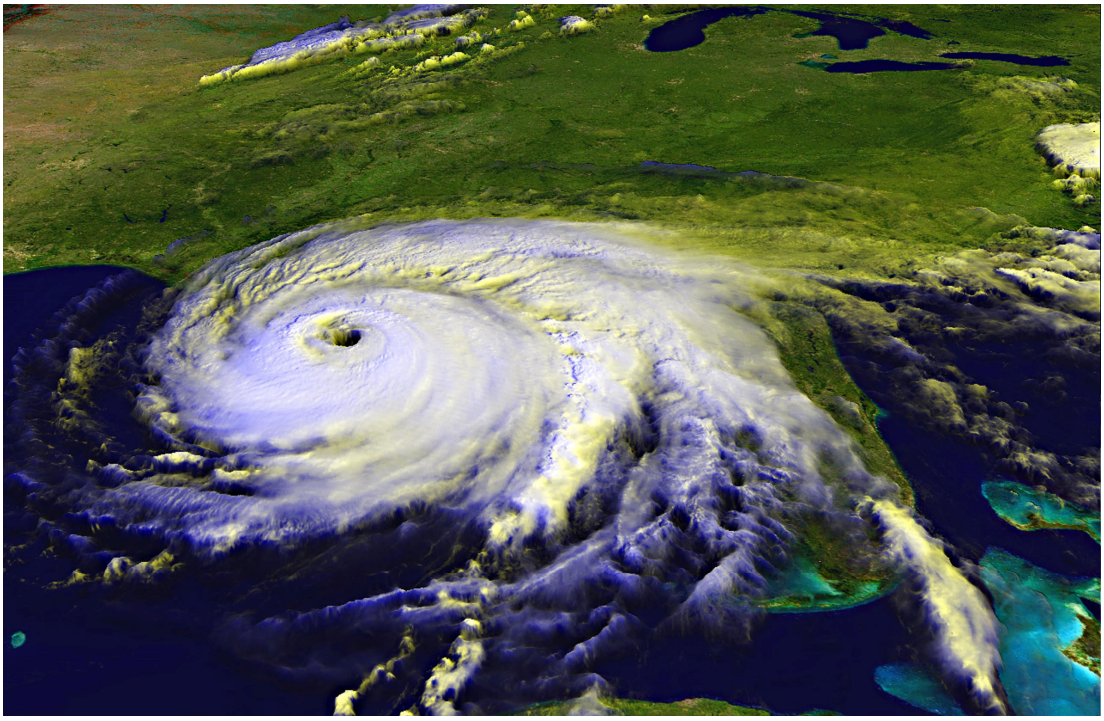

Figure 8.19: Hurricane Ivan in the northern Gulf of Mexico on 16 September 2004.

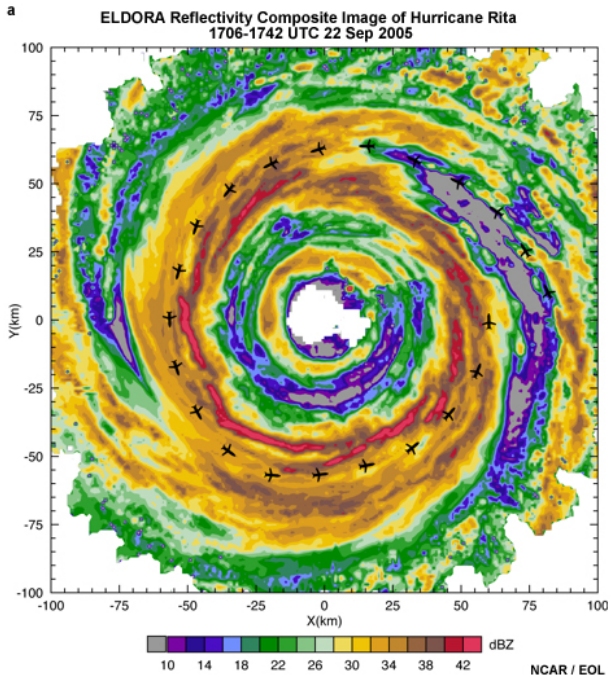

Figure 8.20: Radar reflectivity composite image of Hurricane Rita taken by an airborne radar, 22 Sep 2005, during the Hurricane Rainband and Intensity Change Experiment (RAINEX). The flight track is marked by airplane-shaped markers.

Not all tropical cyclones are as circularly symmetric as seems to be the case in Figures 8.19 and 8.20. Figure 8.21 displays a satellite image of Subtropical Storm Ana on May 8th, 2015. It is hard to visually define where the center of the storm is, and most of the deep convection is located south of what appears to be the circulation center. The surface winds and pressure can also be strongly asymmetric. We will see in Chapter 8 that the interaction between localized potential vorticity anomalies and ambient vertical shear of the horizontal wind is often the source of asymmetries, and most tropical cyclones exhibit varying degrees of asymmetry at different times during their lives.

Figure 8.22 displays a vertical cross-section of reflectivity from a radar aboard an airplane located in the eye of the storm. The eye itself is mostly free of radar returns, except within a few hundred meters of the sea surface, where light precipitation from shallow clouds and perhaps sea spray provide some reflection. The eye is surrounded by very deep, outward-sloping intense radar echoes comprising the eyewall. Allowing for the vertical exaggeration of the graphic, the eyewall slope is roughly 1:1. Stratiform rain from dense clouds in the upper tropospheric outflow is particularly evident on the right side of the diagram, and precipitation from shallow convective clouds is evident outside the eyewall.

Tropical cyclones usually develop visible eyes when their peak winds reach 30-40 ms^{-1} and lose them during rapid dissipation or when the peak surface winds become sufficiently weak.

A view of the eye of a hurricane from the vantage of a hurricane reconnaissance aircraft is shown in Figure 8.28. The deep blue sky of the stratosphere is visible above the spectacular, outward sloping eyewall, and low cumulus and stratocumulus clouds can be seen in the base of the eye. The whole view resembles that of an enormous white coliseum. The diameters of the visible eyes of well-developed hurricanes span two order-of-magnitude, from a few kilometers to several hundred kilometers.

The strongly cyclonic tropical cyclone flow is associated with an intense, localized surface pressure minimum as shown in Figure 8.24. The pressure gradients across the eyewall can be extreme; for example, a gradient of 2.5 hPa/km was measured in Typhoon *Haiyan* just after it made landfall in the Philippines in 2018.

8.4.2 Kinematic and thermodynamic structure

The airflow and thermodynamic properties of tropical cyclone have been measured by research aircraft beginning in the mid 1940s. These aircraft usually deploy instruments on parachutes known as dropwindsondes; today these carry GPS chips and are tracked, yielding estimates of the horizontal wind, while sensors on the sondes radio information about temperature, humidity, and pressure back to the aircraft. Today, highly accurate measurements of airflow in the core of the storm can be made using airborne Doppler radar, which measures the velocity of the reflectors towards and away from the aircraft. By viewing the same reflectors from different angles as the aircraft flies past, two components of the velocity can be obtained and, after correcting for the fall speed of the reflectors, the third wind component may be deduced from mass continuity.

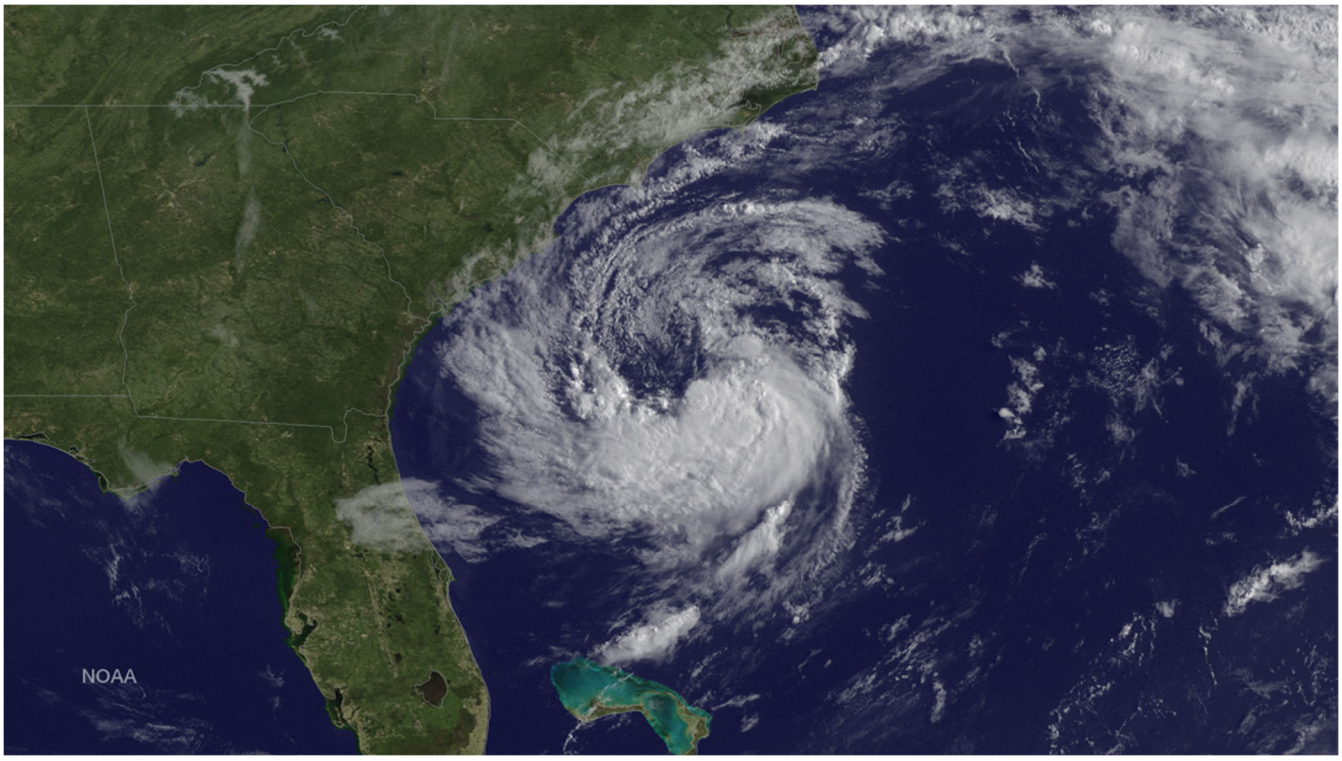

Figure 8.21: Subtropical Storm Ana developing off the U.S. southeast coast on May 8, 2015, as observed by the GOES east satellite.

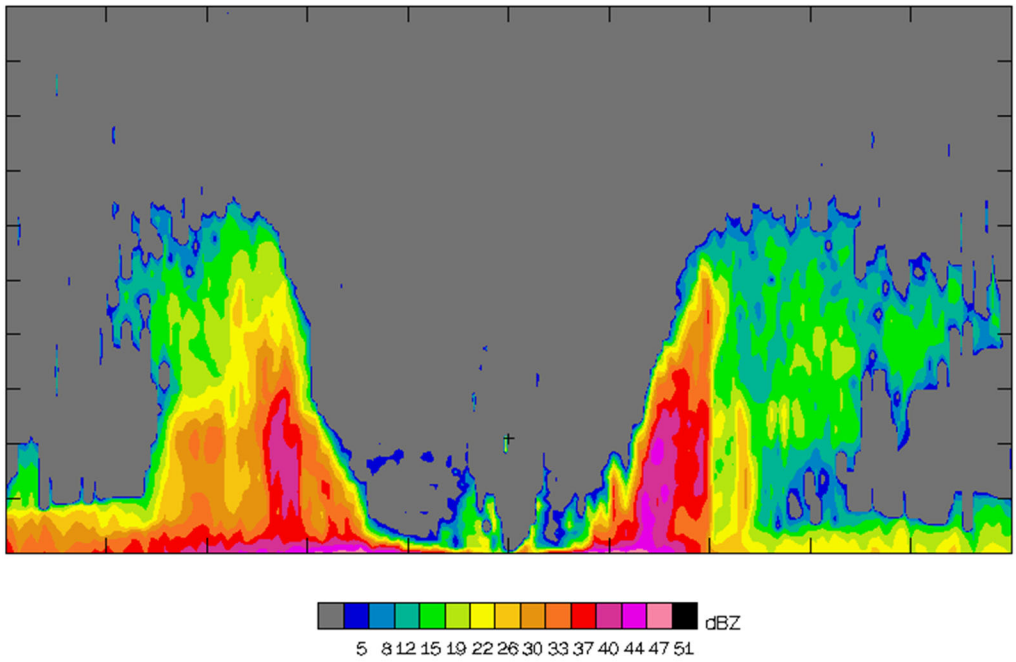

Figure 8.22: Vertical cross section of radar reflectivity in Hurricane Floyd of 1999, made from hurricane reconnaissance aircraft in the eye, located at the "+" sign. The diagram spans 20 km in height and is 120 km across.

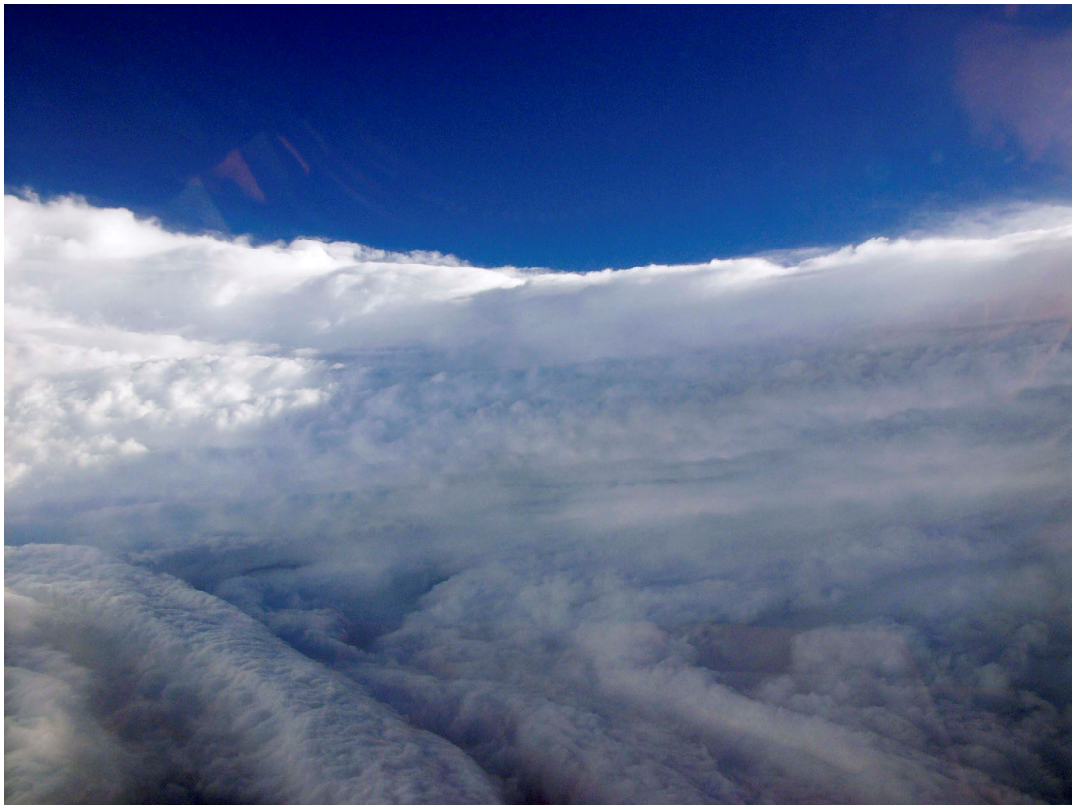

Figure 8.23: View of the eye of Hurricane Katrina on August 28th, 2005, as seen from a NOAA WP-3D hurricane reconnaissance aircraft.

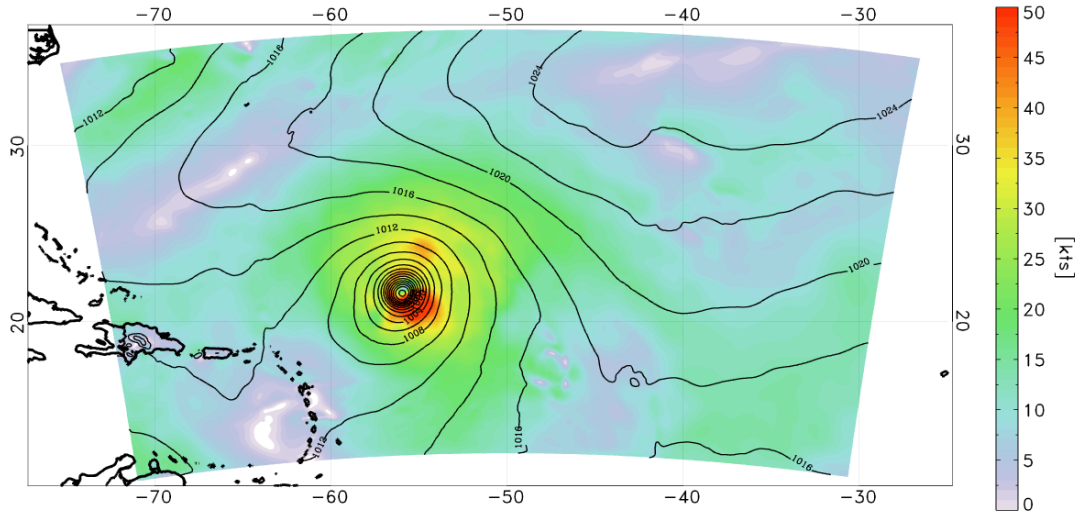

Figure 8.24: Surface pressure distribution associated with a numerically simulated tropical cyclone in the North Atlantic.

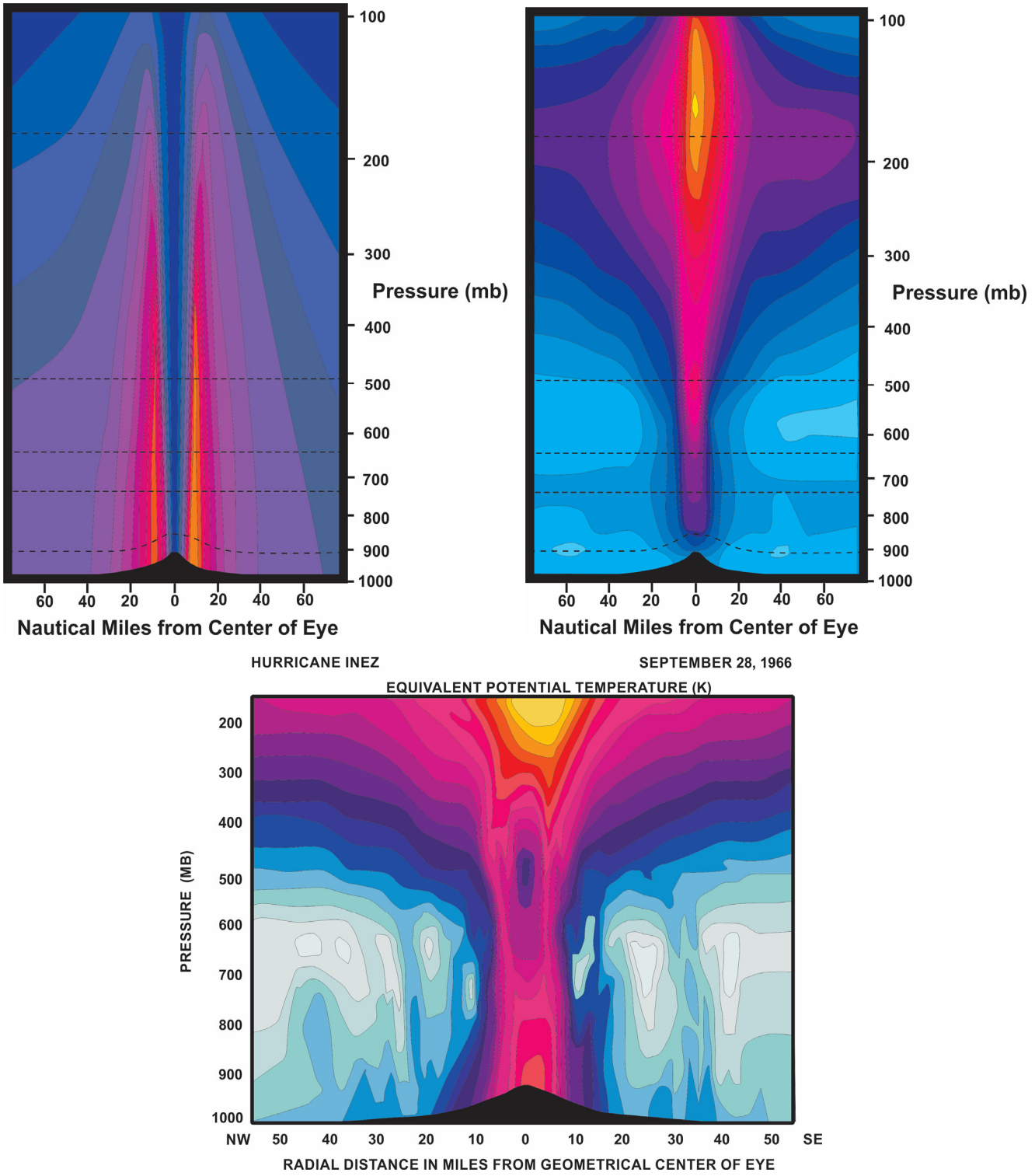

Figure 8.25: Distribution of various quantities in Atlantic Hurricane Inez of 1966. a) azimuthal velocity, from 10 knots to 130 knots with a contour interval of 10 knots; b) temperature anomaly from environment at the same altitude, from 0 K to 16 K with a contour interval of 1K; c) equivalent potential temperature from 336 K to 376 K with a contour interval of 2 K. Cross-sections constructed from data collected by aircraft along the dashed lines in a) and b) and from dropsondes deployed therefrom. After Hawkins and Imbembo (1976)

Cross-sections of wind, temperature, and equivalent potential temperature through an Atlantic hurricane are displayed in Figure 8.25. These have been made from measurements aboard a research aircraft flying at five levels shown by the dashed lines in Figures 8.25 a) and b), supplemented with measurements made from dropwindsondes deployed from the aircraft.

The strongest winds are quite close to the surface (we will have more to say about this and other aspects of the boundary layer in Chapter 4) and decay upwards toward the tropopause. The azimuthal wind increases somewhat linearly from the central axis outwards to the radius of maximum winds, and a close inspection of Figure 8.25a reveals that the RMW slopes outward with height.

Winds decay gracefully away from the RMW, at first roughly following a $r^{-1/2}$ power law, but further out the flow decays somewhat faster and the storm winds vanish at a finite radius (Chapter 4).

There are hardly any variations in air temperature along the surface (Figure 8.25b), though more recent and detailed measurements of the boundary layers of tropical cyclones tend to show some cooling near the RMW, perhaps owing to evaporation of sea spray and rain, direct sensible enthalpy transfer by rain falling through the vertical air temperature gradient, and some cooling due to mixing of the upper ocean (Chapter 7). But aloft the tropical cyclone has a surprisingly hot core, reaching an anomaly of 16 K over the undisturbed environment in the case of Hurricane Inez. The highest temperature anomaly is usually located on the central axis near the level of the ambient tropopause. We will see in Chapter 4 that the warmth of the eyewall directly reflects the enthalpy gained from the ocean by inflowing boundary layer air, while the extraordinary temperatures of the eye itself arise from mechanically forced subsidence, reflecting a small reverse heat engine operating within the eye. The warm-core character of tropical cyclones implies, through hydrostatic balance, that the very low surface pressure anomaly associated with the storm decays with altitude; in fact, a broad anticyclone is usually present close the storm top.

The distribution of equivalent potential temperature (θ_e) in Hurricane *Inez* is shown in Figure 8.25c. This is a quantity whose logarithm is proportional to the entropy of a mixture of dry air, water vapor, and condensed phase water, all assumed to be in thermodynamic equilibrium with each other (Chapter 4). It is conserved for reversible transformations regardless of phase changes of water; its main source in a tropical cyclone is enthalpy transfer from the surface to the atmosphere, which is the driver of the tropical cyclone heat engine. This source is reflected in the strong radially inward gradient of θ_e near the storm center. On the scale of Figure 8.25c it is reasonable to suppose that θ_e is conserved above the boundary layer, but ultimately, the excess entropy flowing out of the top of the storm is lost by infrared radiation to space. Air flowing radially inward turns upward at the eyewall and, supposing the system to be in a steady state, would flow along the contours of θ_e in Figure 8.25c, gradually turning outward near the storm top.

The impressive high-θ_e chimney in Figure 8.25c is a direct signature of the physics of the storm, a giant machine sucking heat out of the warm tropical surface and expelling it into the cold reaches of the upper troposphere. We will have more to say about this in Chapter 4.

The radial and vertical velocity components in tropical cyclones are generally noisier and thus more difficult to measure than the azimuthal flow, though the radial flow in the boundary layer can be quite strong. For this reason, we display in Figure 8.26 time-averaged radial and vertical velocities from a numerical simulation using a nonhydrostatic (convection-permitting) axisymmetric model (Rotunno and Emanuel, 1987). The model is run on a grid with 8.75 km radial and 312.5 m vertical grid spacing, and the quantities shown in the figure have been averaged over one day of a simulation that has reached a quasi-steady state.

At the most basic level, the secondary circulation of a steady-state tropical cyclone consists of radial inflow, mostly confined to a turbulent boundary layer of a few hundred meters to perhaps 2 km in thickness, intensifying inward to a maximum outside the eyewall and then rapidly decaying to approximately zero just inside the eyewall as the bulk of the flow turns upward into a strong eyewall updraft. In the exceptionally intense vortex shown in Figure 8.26, the time-mean eyewall updraft reaches a peak speed of about 8 ms^{-1} at around 11 km altitude, then decreasing upward as the flow turns radially outward. The outflow in this simulated storm reaches a peak magnitude of about 20 ms^{-1} not far outside the core of the storm. The outflow layer, near the level of the ambient tropopause, progressively thins with radius. In an axisymmetric framework such as used here, the outflow takes much longer to become quasi-steady, if I does so at all, because there are no explicit three-dimensional eddies to add angular momentum to the outflow, to balance the persistent outward advection of the low angular momentum originating in the storm's core.

The simple in-up-and out circulation is augmented by a curious secondary inflow just below the primary outflow layer, visible in Figure 8.26a. This begins outward of 800 km at an altitude of about 14 km, and slopes inward and downward, reaching a peak magnitude of about 5 ms^{-1} just outside the eyewall, at an altitude of about 8 km. The axis of this elevated inflow layer more or less follows a surface of constant absolute angular momentum (Figure 8.27) and may be driven by the evaporation of precipitation falling from dense stratiform cloud in the outflow layer above it.

Note in Figure 8.26 the very sharp horizontal gradients of both the radial and vertical velocities along the inner edge of the eyewall updraft. In many places most of the total change from the small values within the eye itself to the maximum value in the eyewall region occurs over a single model grid interval. As we will show in Chapter 5, the eyewall is strongly frontogenetical. Note also in Figure 8.26b that the eyewall updraft slopes outward, and that in this finite-difference model, the outward slope is accomplished by a series of outward steps at various altitudes.

Physical systems are most concisely described using conserved variables. We have already introduced one essential conserved thermodynamic variable the equivalent potential temperature (θ_e; Figure 8.25c). For axisymmetric flows, a very useful conserved dynamical variables is the absolute angular momentum per unit mass, M:

$$M \equiv rV + \Omega \sin\theta r^2, \qquad \textbf{(1)}$$

Where r is the radius, V the azimuthal component of the velocity, Ω is the planetary angular rotation rate, and θ the latitude.

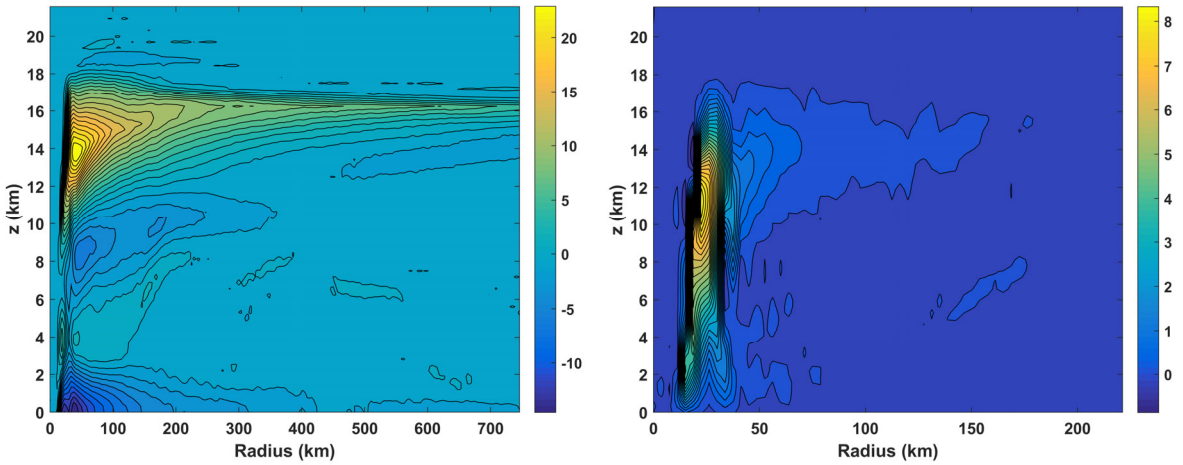

Figure 8.26: Radial-vertical section of radial (a) and vertical (b) velocities (ms^{-1}) averaged over one day during the quasi-steady phase of a tropical cyclone simulated using the axisymmetric, nonhydrostatic model of Rotunno and Emanuel (1987). Note that the radial scale in (b) is roughly one third that of (a).

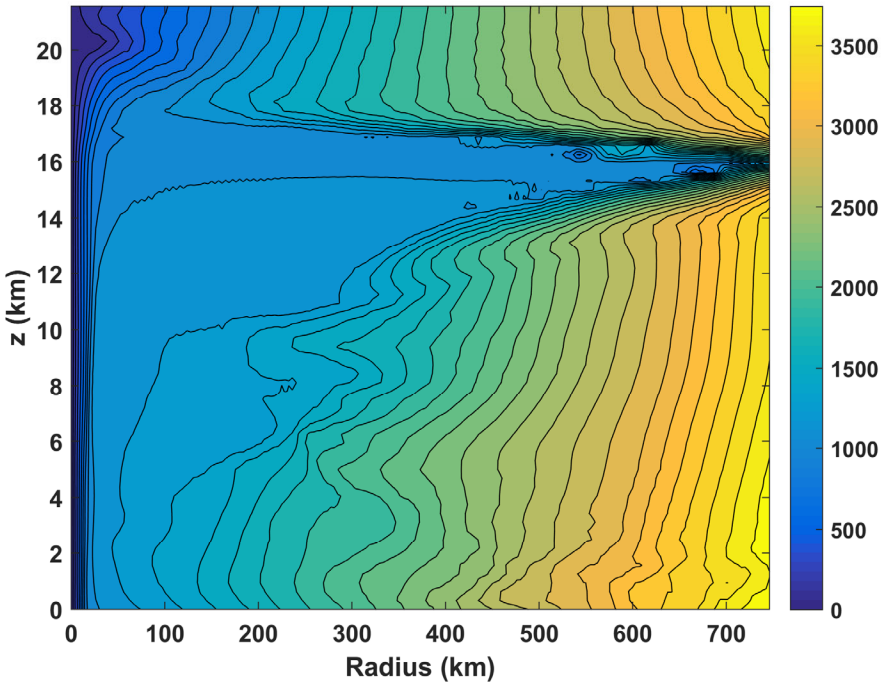

Figure 8.27: Radial-vertical section of the distribution of the square-root of the angular momentum given by equation (1).

The distribution of angular momentum in the numerically simulated storm used to construct Figure 8.26 is displayed in Figure 8.27. (Here the square root of M is shown to bring out more detail in the inner core region.) Bearing in mind that the undisturbed angular momentum surfaces are vertical cylinders centered at the storm center, the inward deflection of the surfaces reflects the cyclonic winds of the storm. The most prominent feature of the angular momentum distribution is the outward protrusion of low values of M near the tropopause, corresponding to strongly anticyclonic flow near the storm top.

The strong radial inflow in the boundary layer clearly crosses M surfaces, and assuming that the flow is steady, this reflects the loss of angular momentum owing to the torque exerted by the surface upon the cyclonic flow. By the time the inflow reaches the eyewall, it has lost much of its original angular momentum, and this low M air then flows up the eyewall and out near the tropopause. Assuming that the flow at the top of Figure 8.27 (in the lower stratosphere, around 22 km) nearly vanishes, and following the M surfaces downward to the outflow layer, one can see that they deflect inward into the outflow inside of about 400 km radius, corresponding to cyclonic flow, and outward outside 400 km, indicating anticyclonic flow. The thin but powerful anticyclonic lens near the tropopause is a highly prominent feature of developed tropical cyclones. In the real world, the anticyclone is usually displaced from the cyclone beneath it by environmental wind shear, and the outflow can be highly three-dimensional, often focused into curved jets. Figure 8.28 shows outflow streamlines in two numerically simulated tropical cyclones, one in a calm ambient environment and another in which there is both horizontal and vertical shear of the ambient horizontal wind (Rappin et al., 2011). In the first case, the outflow is quite axisymmetric, but when ambient shear flow is present, much of the outflow is focused into an anticyclonically curved jet north of the storm center. Flow at upper levels in association with a western North Pacific typhoon is shown in Figure 8.29. In this case, the outflow is focused into two anticyclonically curved jets, one north and one south of the storm center. The strong interaction of tropical cyclone outflow with other weather systems is evident in this figure, which is typical of real tropical cyclones, especially as they move into higher latitudes.

8.4.3 The eye

The circulation in the eye of a tropical cyclone is especially unusual and interesting. Figure 8.30 shows a sketch of the secondary airflow in and near the eye of a mature storm, based on observations and numerical simulations. The primary circulation is cyclonic, with azimuthal velocity increasing outward to its maximum value in the eyewall. During rapid intensification, the azimuthal velocity can be near zero through much of the eye, increasing very abruptly just inside the eyewall. In this case, the absolute value of the vertical component of vorticity has a sharp peak in the eyewall, and as well shall review in Chapter 6, this flow arrangement can be highly unstable to three-dimensional eddies, which are known to exist in real storms and often made visible by shallow clouds in the eye (Figure 8.31).

When the storm is nearly steady, the temperature in the eye is highly elevated, decreasing radially outward from a maximum on the central axis. Air gently subsides in the center of the eye, with compressional heating balanced by infrared radiative cooling to space. Subsidence velocities are two orders of magnitude smaller than ascent rates in the eyewall, averaging around $1\ cm\,s^{-1}$. Stronger subsidence is found just inside the eyewall, where surfaces of constant potential temperature slope upward in association with negative radial temperature gradients, allowing air to descend along inward-sloping trajectories, more nearly adiabatically than is possible in the center of the eye.

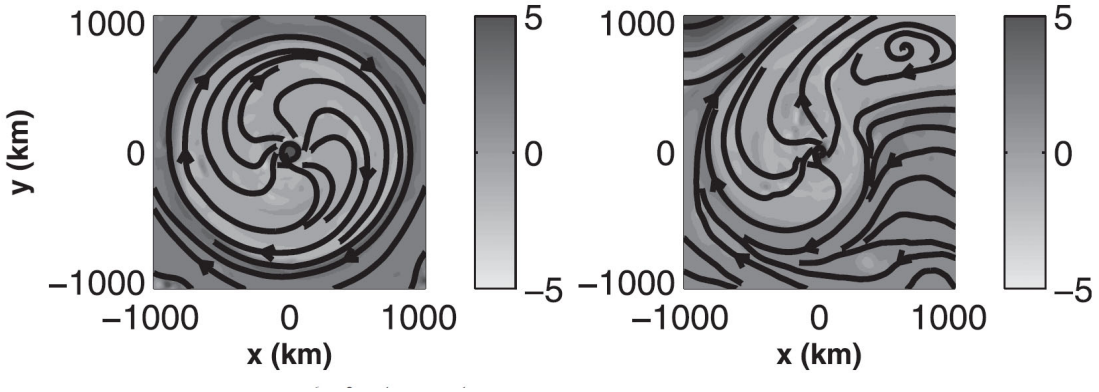

Figure 8.28: Streamlines (black) and potential vorticity (gray-shaded) at 13 km altitude in numerical simulations of tropical cyclones with constant Coriolis parameter in a calm environment (left) and in an environment with an ambient west-to-east jet stream north of the cyclone center (right). From Rappin et al. (2011)

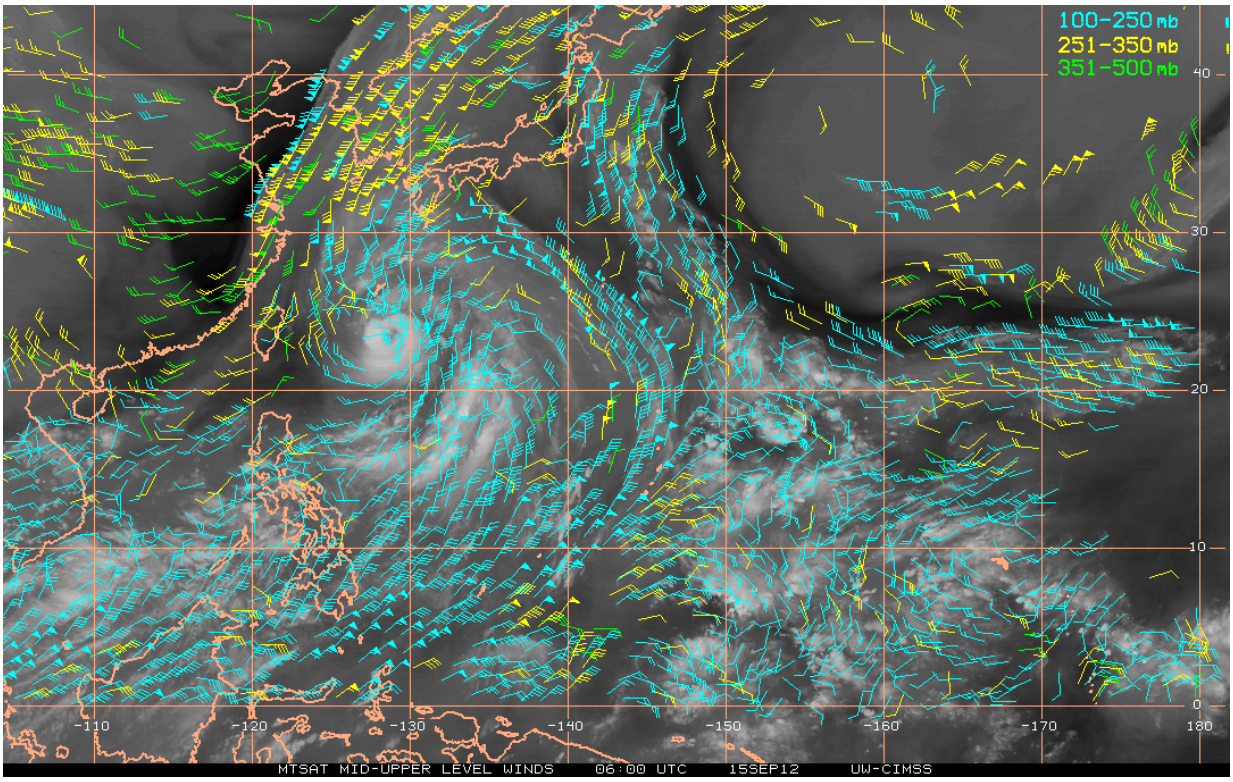

Figure 8.29: Airflow at three levels, indicated in the upper right, at 06 UTC on 15 September 2012 over the western North Pacific in association with Typhoon Sanba seen in the center left portion of the image. Note that the outflow is concentrated into two, anticyclonically curving jets.

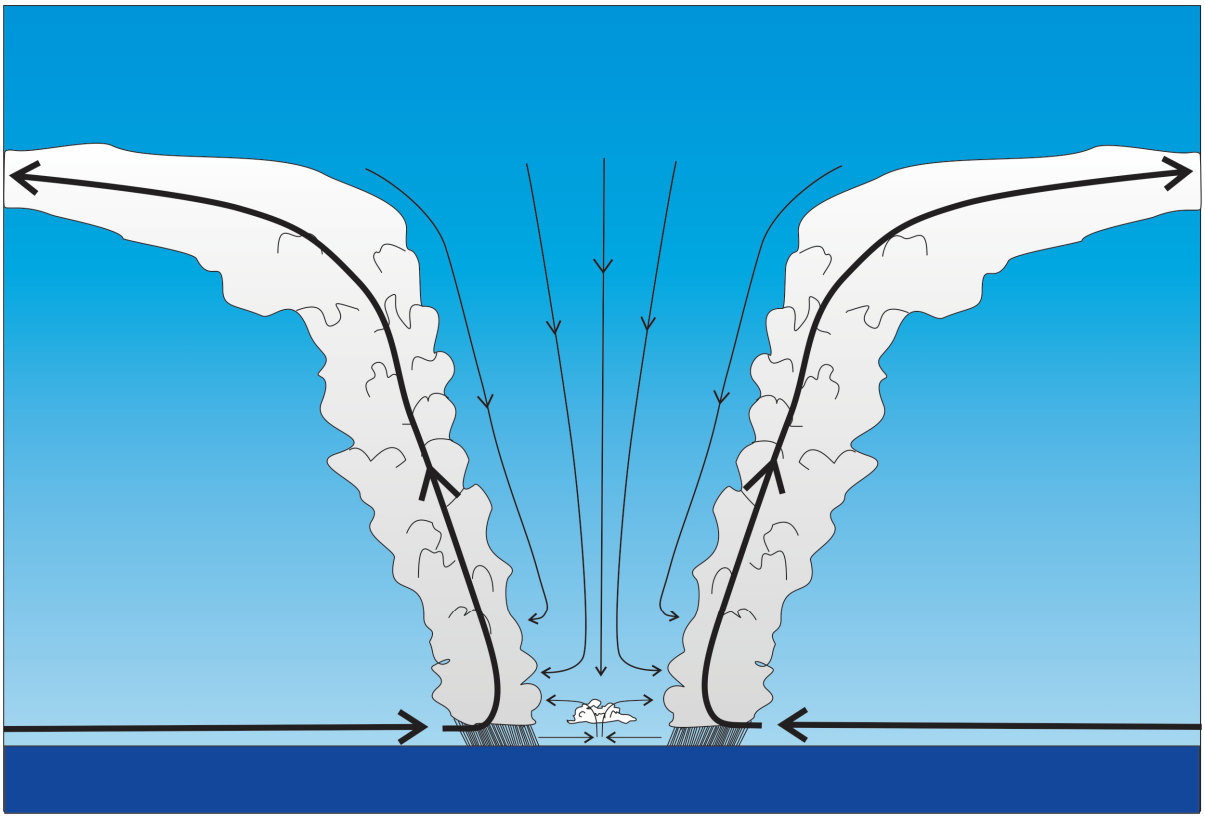

Figure 8.30: Schematic cross-section of airflow in the eye of a mature tropical cyclone. Bold arrows denote the main secondary circulation while the thin arrows denote airflow in the eye itself.

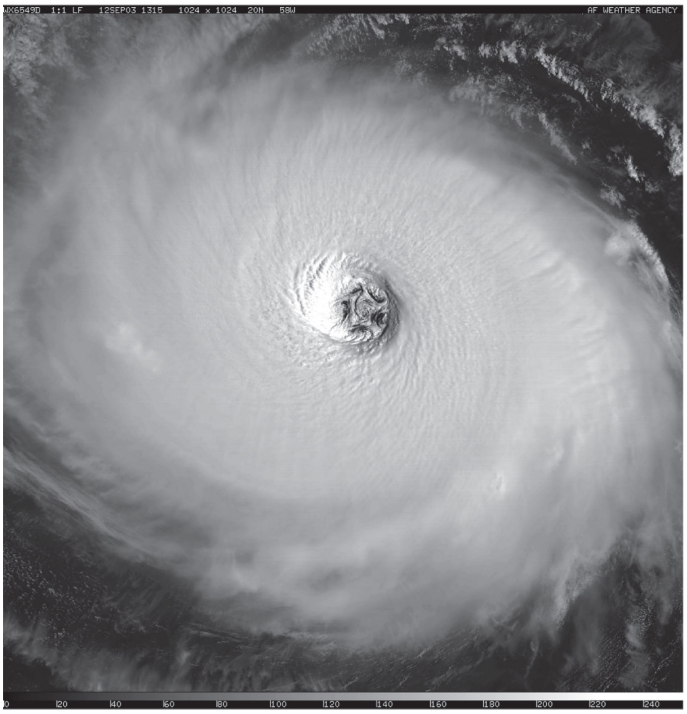

Figure 8.31: View of the eye of Atlantic Hurricane Isabel on 12 September, 2003, from a Defense Meteorological Program satellite

The eyewall eddies also transport cooler air and hydrometeors into the eye, allowing the compressional heating to be balanced by advective and evaporative as well and radiative cooling. Descent rates near the inner edge of the eyewall can reach many $cm\,s^{-1}$.

Because the boundary layer airflow is cyclonic, the torque exerted on it by surface friction causes an inward Ekman flow, just as in the eyewall and outer regions of the storm. But the very large inertial stability of the eye means that only a small radial velocity (a few ms^{-1}) is needed to balance the surface torque. Convergence of this radial Ekman flow leads to a weak, shallow updraft often made visible by a formation of shallow cumulus or stratocumulus clouds near the central axis; this is sometimes referred to as the *hub cloud*.

Where the shallow, relatively cool updraft meets the hot, downward flowing air, remarkably strong temperature inversions develop. The two air streams turn radially outward, toward the eyewall. The radial outflow crosses tightly packed surfaces of constant angular momentum; this is made possible by the inward transport of angular momentum by three-dimensional eddies.

The eye circulation above the boundary layer is thermally indirect, with relatively warm air sinking, and constitutes a giant reverse heat pump, driven mechanically by inward eddy transport of eyewall angular momentum, as we will discuss in detail in Chapter 6.

During episodes of rapid intensification, the eye itself is gradually spun up by three-dimensional eddies, accompanied by descent rates that may be substantially stronger than those associated with the steady state. The temperature inversion in the eye may at such times descend to quite low levels in response to the strong subsidence. Conversely, during periods of rapid weakening (for example, after the storm passes over land) the angular velocity of the eye may temporarily exceed that of the eyewall, causing an outward eddy flux of angular velocity and a reduced descent or even ascent in the eye. During such times, the boundary layer can deepen dramatically and the eye may fill with cloud.

8.4.4 Associated phenomena

8.4.4.1 Waves

The strong surface winds of tropical cyclones create very high amplitude ocean waves, and the rapid shift in wind direction near the storm center can create confused and dangerous sea states. For example, high seas associated with a western Pacific typhoon sank two destroyers and damaged much of the rest of Admiral Halsey's U.S. Third Fleet in December of 1944, near the end of World War II. Significant wave heights[5] in excess of 12 m have been reported, and individual wave heights can approach 35 m. Figure 8.32 displays the amplitude, direction and wavelength of ocean surface waves associated with Hurricane *Bonnie* of 1998 (Wright et al., 2001). The largest and steepest waves generally occur to the right of the storm track (left in the Southern Hemisphere). The wave field is strongly influenced by the intensity and geometry of the storm, its translation speed, and pre-existing ocean currents. Near shore, the wave field is made even more complex by refraction from coastlines.

[5] Generally, the average of the uppermost 1/3 of the probability distribution of trough-to-crest wave heights.

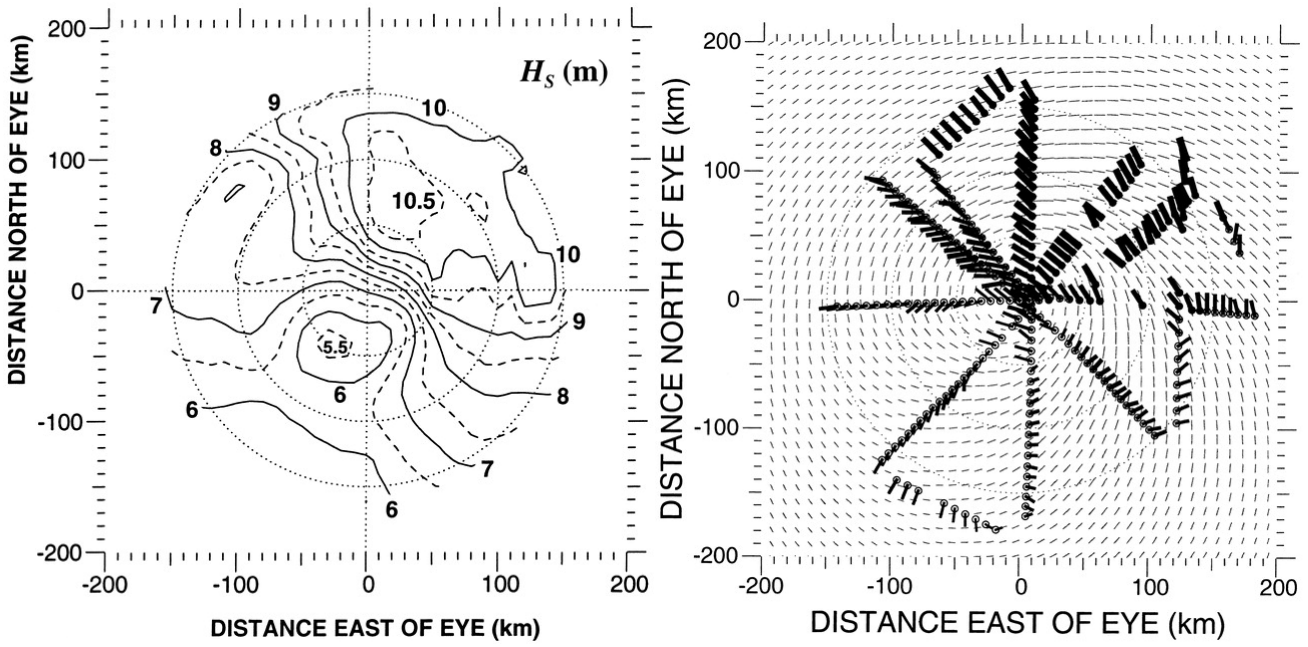

Figure 8.32: (a) Spatial variation in significant wave height measured by a scanning radar altimeter in Hurricane Bonnie on 24 Aug 1998. Contours for integer values of wave height (in meters) are solid and contours for integer values plus 0.5 m are dashed. Bonnie was moving toward the northwest at this time. (b) Hurricane Bonnie primary wave field. The circles indicate the data locations and the radials extend in the wave propagation direction a length proportional to the wavelength. The width of the radials is proportional to the significant wave height, so the aspect ratio is an indication of wave steepness. The short, narrow lines indicate the HRD surface wind analysis. Wright et al. (2001).

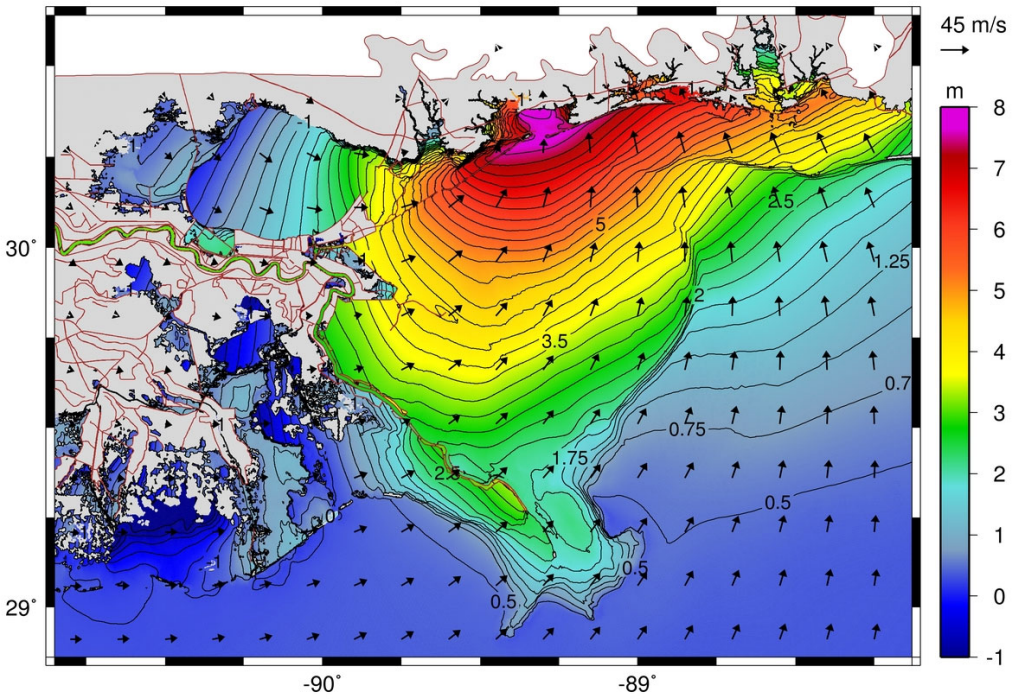

Figure 8.33: Surge heights in Hurricane Katrina as simulated by the Advanced Circulation Model (ADCIRC) of the Computational Hydraulics Laboratory at the University of Notre Dame. Black arrows indicate wind direction and speed.

8.4.4.2 Storm Surges

Storm surges are rapid rises in sea level that accompany tropical cyclones. They are responsible for most deaths and large damages from these storms. They are hydrodynamically nearly identical to tsunamis but they are driven by winds rather than moving sea floor. For this reason, storm surge damage resembles damage from tsunamis, with ships and debris swept far inland.

Technically, the *storm surge* is the storm-driven rise of the sea over and above the predicted astronomical tide at the date and location of the event. The *storm tide* is the total storm-driven rise of water including both the surge and the astronomical tide. Flooding depends on the storm tide and thus, of course, on the state of the astronomical tide when the surge strikes. Where astronomical tides are associated with strong currents, the surge and the tide cannot be considered independently, as tidal currents affect the dynamics of the surge, so the storm tide is not always approximated by the arithmetic sum of the normal astronomical tide and the wind-drive surge. Figure 8.33 shows a numerically simulated storm surge accompanying Hurricane Katrina of 2005, the largest surge ever recorded along the U.S. coastline. Strong effects of the complex coastal geography are evident, and the peak surge is to the east of the storm track (not shown in this figure). The hydrodynamics of storm surges are well understood and simulated, as will be discussed in Chapter 8, and the main uncertainties in forecasting surges arise from errors in forecasting the storm track, intensity, size and timing relative to astronomical tides.

8.4.4.3 Tornadoes

As if high winds, floods, and storm surges were not enough, landfalling tropical cyclones often produce tornadoes, which can do considerable damage. Most of these occur in the right-front (left-front in the southern hemisphere) quadrant of the storm with respect to its direction of motion (Figure 8.34) and within 600 km inland of the point of landfall (Schultz and Cecil, 2009). A detailed analysis of the thermodynamic and kinematic environments of tropical-cyclone spawned tornadoes shows that there is far less buoyancy available than is typical of supercell-type thunderstorms of the type responsible for most destructive tornadoes, but this is compensated by strongly varying low-level wind shear, giving rise to storm with very high values of helicity (McCaul Jr., 1991). The strong low-level wind shear is produced by surface drag acting on the strong low-level gradient winds of tropical cyclones.

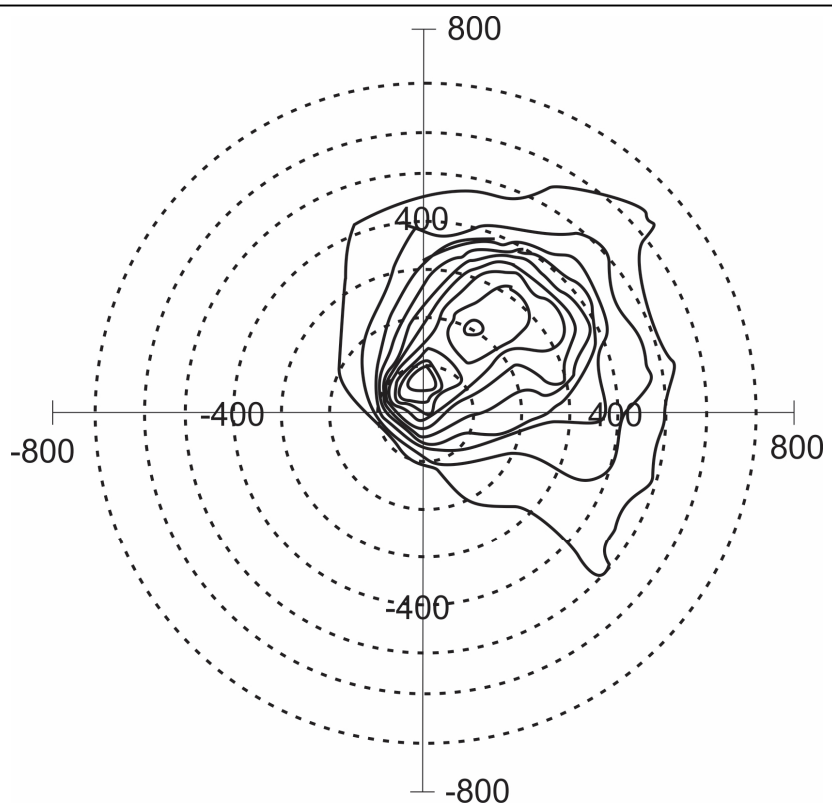

Figure 8.34: Two-dimensional histogram of tornado occurrence relative to storm motion vector (pointing toward top of page). The circles show distance from storm center in increments of 100 km and the contours are in intervals of 10 tornadoes per 100 km^2 bin spacing. After Schultz and Cecil (2009).

References

Cavicchia, L., H. Von Storch, and S. Gualdi, 2014: A long-term climatology of medicanes *Clim. Dyn.*, **48.**

Chavas, D. R., and K. A. Emanuel, 2010: A QuickSCAT climatology of tropical cyclone size. *Geophys. Res. Lett.*, **37**. 10.1029/2010GL044558.

Dean, L., K. Emanuel, and D. R. Chavas, 2009: On the size distribution of Atlantic tropical cyclones. *Geophy. Res. Lett.*, **36**. 10.1029/2009GL039051.

Emanuel, K., J. Callaghan, and P. Otto, 2008: A hypothesis for the re-development of warm-core cyclones over northern Australia. *Mon. Wea. Rev.*, **136,** 3863-3872.

Evans, C., R. S. Schumacher, and T. J. Galarneau Jr., 2011: Sensitivity in the overland reintensification of Tropical Cyclone Erin (2007) to near-surface soil moisture characteristics. *Mon. Wea. Rev.*, **139,** 3848-3870.

Hawkins, H. F., and S. M. Imbembo, 1976: The structure of a small, intense hurricane-Inez 1966. *Mon. Wea. Rev.*, **104,** 418-442.

Huffman, G. J., and co-authors, 2007: The TRMM Multisatellite Precipitation Analysis (TMPA): Quasi-global, multiyear, combined-sensor precipitation estimates at fine scales. *J. Hydrometeor.*, **8,** 38-55.

Jiang, H., and E. J. Zipser, 2010: Contribution of tropical cyclones to the global precipitation from eight seasons of TRMM data: Regional, seasonal, and interannual variations. *J. Climate*, **23,** 1526-1548.

Kossin, J. P., and Coauthors, 2007: Estimating hurricane wind structure in the absence of aircraft reconnaissance. *Wea. and Forecast.*, **22,** 89-101.

McCaul Jr., E. W., 1991: Bouyancy and shear characteristics of hurricane-tornado environments. *Mon. Wea. Rev.*, **119,** 1954-1978.

Rappin, E. D., M. C. Morgan, and G. J. Tripoli, 2011: The impact of outflow environment on tropical cyclone intensification and structure. *J. Atmos. Sci.*, **68,** 177-194.

Romero, R., and K. Emanuel, 2013: Medicane risk in a changing climate. *J. Geophys. Res.*, **118**. doi:10.1002/jgrd.50475.

Rotunno, R., and K. A. Emanuel, 1987: An air-sea interaction theory for tropical cyclones. Part II. *J. Atmos. Sci.*, **44,** 542-561.

Schultz, L. A., and D. J. Cecil, 2009: Tropical cyclone tornadoes, 1950-2007. *Mon. Wea. Rev.*, **137,** 3471-3484.

Tang, S., R. K. Smith, M. T. Montgomery, and M. Gu, 2016: Numerical study of the spin-up of a tropical low over land during the Australian monsoon. *Quart. J. Roy. Meteor. Soc.*, **142**. DOI: 10.1002/qj.2797.

Wright, C. W., and Coauthors, 2001: Hurricane directional wave spectrum spatial variation in the open ocean. *J. Phys. Ocean.*, **31,** 2472-2488.

Yanase, W., and co-authors, 2016: Climatology of polar lows over the Sea of Japan using the JRA-55 reanalysis. *J. Climate*, **29,** 419-437.

Zhan, M., and H. von Storch, 2008: A long-term climatology of North Atlantic polar lows. *Geophy. Res. Lett.*, **35**. doi:10.1029/2008GL035769.